Interleukin-13 Activates Distinct Cellular Pathways Leading to Ductular Reaction, Steatosis, and Fibrosis

Immunity

IL-13 Activates Distinct Cellular Pathways Leading to Ductular Reaction, Steatosis, and Fibrosis

--Manuscript Draft--

Manuscript Number:	IMMUNITY-D-15-00701R2
Full Title:	IL-13 Activates Distinct Cellular Pathways Leading to Ductular Reaction, Steatosis, and Fibrosis
Article Type:	Research Article
Keywords:	fibrosis; regeneration; interleukin-13; Hepatic Progenitor Cell; liver; Steatosis; Ductular Reaction; Cholestasis
Corresponding Author:	Thomas A. Wynn Bethesda, MD UNITED STATES
First Author:	Richard Lee Gieseck III
Order of Authors:	Richard Lee Gieseck III
	Thirumalai R Ramalingam
	Kevin M Hart
	Kevin M Vannella
	David A Cantu
	Wei-Yu Lu
	Sofía Ferreira-González
	Stuart J Forbes
	Ludovic Vallier
	Thomas A Wynn
Abstract:	Fibroproliferative diseases are driven by dysregulated tissue repair responses and are a major cause of morbidity and mortality as they affect nearly every organ system in the body. Type-2 cytokine responses (interleukin-4 and interleukin-13) are critically involved in tissue repair; however, the mechanisms that regulate repair versus pathological fibrosis are not well understood. Here, we show that the type-2 effector cytokine interleukin-13 simultaneously, yet independently, directs hepatic fibrosis and the compensatory proliferation of hepatocytes and biliary cells in progressive models of liver disease induced by IL-13 over-expression or following infection with Schistosoma mansoni. Using conditional mutant mice with interleukin-13 signaling genetically disrupted in hepatocytes, cholangiocytes, or resident tissue fibroblasts, we reveal direct and distinct roles for interleukin-13 in fibrosis, steatosis, cholestasis, and ductular reaction. Together, these studies show that these mechanisms are simultaneously controlled but distinctly regulated by interleukin-13 signaling. Thus, it may be possible to promote IL-13-dependent hepatobiliary expansion without generating pathological fibrosis.
Suggested Reviewers:	Paul W Noble Cedars Sinai Medical Center paul.noble@cshs.org Expertise in type-2 driven fibrosis.
	Dean Sheppard UCSF dean.sheppard@ucsf.edu Expertise of fibrosis of multiple etiologies and organ systems.
	Rebecca G. Wells University of Pennsylvania rgwells@mail.med.upenn.edu

	Expertise in Hepatic FIbrogenesis
	David Brenner UCSD dbrenner@ucsd.edu Expertise in immunological mechanisms of hepatic fibrogenesis.
	Derek Mann Newcastle University derek.mann@ncl.ac.uk Expertise in molecular regulation of tissue fibrosis.
Opposed Reviewers:	Ajay Chawla UCSF Ajay.Chawla@ucsf.edu Competing research interests in the role of type-2 cytokines in hepatic fibrosis and regeneration.

NATIONAL INSTITUTE OF ALLERGY AND INFECTIOUS DISEASES

National Institutes of Health
www.niaid.nih.gov

Dr. Bruce Koppelman, Ph.D.
Scientific Editor
Immunity, Cell Press
50 Hampshire St. 5th floor
Cambridge, MA 02139

April 21, 2016

Dear Dr. Koppelman,

Per our previous discussion, please find attached our revised manuscript entitled "IL-13 Activates Distinct Cellular Pathways Leading to Ductular Reaction, Steatosis, and Fibrosis" (IMMUNITY-D-15-00701). We have included a point-by-point response to reviewer's comments in a separate document and have added additional text to address the editorial concerns you brought to our attention. We believe we have adequately addressed all of the major and minor concerns of the reviewers, in several cases with additional supportive data, so we hope that you will find the revised paper as exciting as we do.

I affirm that all authors concur with its re-submission. The material submitted for publication has not been previously reported and is not under consideration for publication elsewhere.

Sincerely yours,

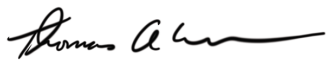

Thomas A. Wynn
Senior Investigator NIH/NIAID
4 Memorial Dr
Bethesda, MD 20892-0425, USA
Ph: 301-496-4758
twynn@niaid.nih.gov

NATIONAL INSTITUTE OF ALLERGY AND INFECTIOUS DISEASES

National Institutes of Health
www.niaid.nih.gov

April 21, 2016

Dear Dr. Koppelman,

Thank you for considering our manuscript for publication in Immunity. We appreciate the reviewers' helpful comments and have addressed the comments below. Additionally, as per our correspondence, we have added additional text citing previous human studies and ongoing clinical trials to emphasize the important pathogenic role of IL-13 in diseases impacting many organs and to place our IL-13 overexpression studies into appropriate context. We believe that our revisions have clarified and solidified the major conclusions of the manuscript, as explained in our point-by-point response below.

REVIEWER SPECIFIC COMMENTS:

1. In the previous critique it was stated " In Figure 1 H, …...At weeks 12 and 18, there seems to be a trend towards lower ALT and AST levels in the AlbCre+ mice but numbers at these time points are extremely low." The authors now state "Our n-values of 17 and 21 mice for Alb-Cre negative and positive respectively have enough power to discern significant differences between the groups", but the numbers in the Alb-Cre positive mice remains n=4 and n=3 at these time points.

We appreciate the reviewer's concern regarding the possible trend at later time points. Previously, we only provided representative results from the week 12 and 18 time points. However, these experiments were replicated on four separate occasions with similar results at multiple time points. The new graph included below and incorporated into a revised Figure 1 now includes pooled results from individual mice at 4, 8, 12, and 18 weeks post-infection. The new graphs clearly show a similar pattern of AST/ALT expression at multiple time points post infection. Additional data points are unlikely to alter the conclusion of these convincing results. As expected, peak AST/ALT levels were observed on week 8 post-infection, when the inflammatory response in the liver reaches a maximum.

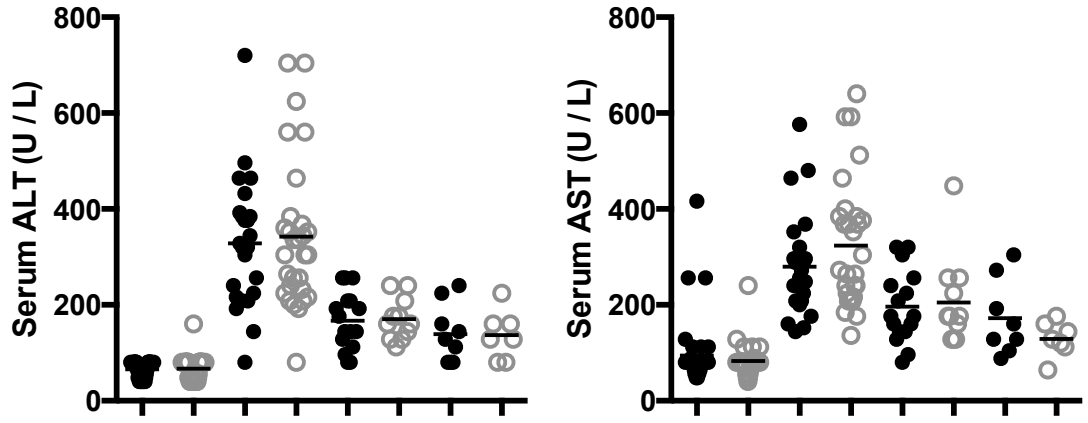

The data shown are week 4, 8, 12, and 18 for Cre negative (black symbols) and Cre positive (open symbols) mice. The additional data points increase the n of the Cre+ week 12 group from 4 to 11 and week 18 from 3 to 7. The data from other experiments also increased the "n" of the two earlier time points as well.

Please refer to the original graphs for comparison:

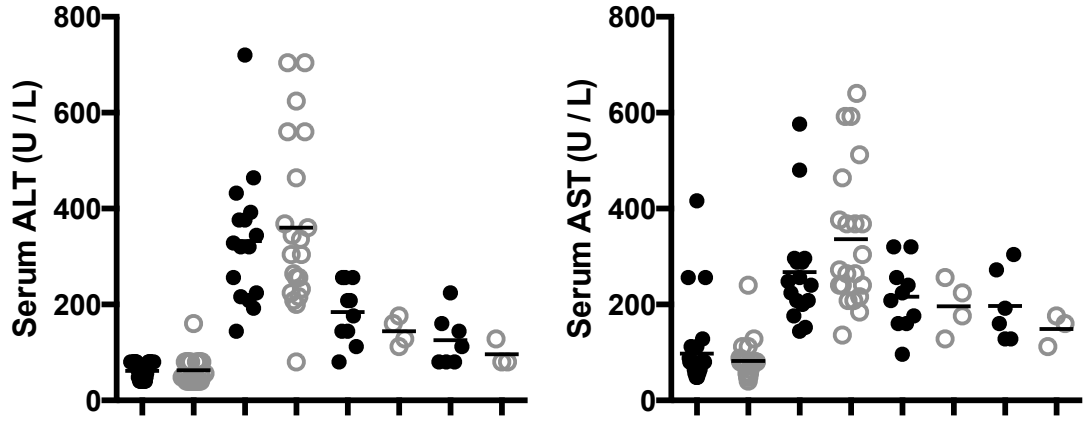

2. The authors continue to use a subtractive approach by comparing results in Alb-Cre positive mice (deleting in hepatocytes and cholangiocytes) and K19-CreERT mice. Previously, this reviewer had requested an AAV8-Cre-based approach as a simple straightforward method for hepatocyte-specific deletion. This approach does not require any additional crosses of mice and vectors are easily available and highly efficient. It is an important and easy-to-do experiment.

statements/headings such as "IL-4/13 Signaling in Hepatocytes and/or Biliary Cells drives DR but not Fibrosis" and "IL-13 Signaling in Hepatocytes and/or Biliary Cells Induces DR and Steatosis, but not

Fibrosis" need to be avoided and the reader really needs to know if a contribution in hepatocytes can be excluded.

Firstly, we would like to point out that the use of the K19-CreERT model (which is specific for biliary lineage, i.e. ductular reaction) alone demonstrates a previously unknown relationship between ductular reaction and fibrosis, namely that in IL-13 driven liver disease, ductular reaction does not trigger fibrosis and fibrosis does not directly induce ductular reaction. This is an important point as most researchers in the field thought that either ductular reaction was driving the fibrosis or conversely that fibrosis was driving ductular reaction. Paired with the data from the PDGFRB-Cre model, we have unequivocally demonstrated that these two phenomena are uncoupled and that the correlation observed between the two is explained by the common driver of both, namely IL-13. The Albumin-Cre mouse deletes the IL-4R in both hepatocytes and biliary cells, while the K19-Cre mouse deletes the IL-4R only in biliary cells. IL-4Ra expression was preserved in hepatocytes in the K19-Cre mouse but ductular reaction was completely prevented in these mice. We obtained nearly identical results with both Cre expressing strains, unequivocally demonstrating that biliary cells but not hepatocytes are critical for epithelial cell proliferation and thus the ductular reaction. Therefore, we do not understand why it is important to further rule out a role for hepatocytes with a second approach when biliary cells were clearly identified as the critical population targeted by IL-13 that causes ductular reaction. The only difference we observed between the Alb-Cre model and K19-CreERT model is a difference in eotaxin expression, which was corroborated by differences in eosinophilic infiltration in our liver histological specimens. This was not a major conclusion of the paper. Furthermore, although often ignored, AAV vectors are potentially problematic as they are known to induce a small, yet detectable, anti-viral immune response (Zaiss et al., 2002), which could complicate the interpretation of results. While the anti-viral response may be small enough to be ignored in some studies, because we are exploring an immunological mechanism of fibrosis, it's possible the anti-viral response will become a complicating factor. We believe that it is highly unlikely that the proposed AAV-Cre model experiment suggested by the reviewer will produce different results.

3. Recombination efficiency of PDGFRB-Cre needs to be confirmed. There is a big difference between fluorescent reporters and each recombined gene, and it is absolutely necessary to precisely quantify how efficiently IL4Rαflox/flox is deleted in hepatic stellate cells.

We reiterate that the highly significant phenotypes shown in Figure 5, combined with previous studies assessing efficiency clearly suggest a very high level of recombination of IL4Ra. However, we have since performed isolation of HSCs and genomic DNA genotyping to confirm the recombination efficiency. As expected, the efficiency approaches 100% and thus these new data do not change the conclusions of the manuscript.

4. Addition of a second model as suggested by this reviewer and reviewer #2 (BDL, DDC or NASH) is important and has not been addressed in the revision. The statement by the authors "it seems a bit unfair to

ask us to now duplicate the studies with several additional models of liver disease" is not well taken. Some of these models, e.g. DDC diet, are very quick and all mice should be in place. At minimum, the authors could have done studies in one additional model, in particular since reviewer #2 made similar requests.

According to the World Health Organization liver cirrhosis (LC) is considered a major public health threat, with approximately 800,000 people dying from LC every year. In the United States alone, LC is responsible for around 27,000 deaths per year, representing a mortality rate of 9.2 per 100,000, placing it as the 12th overall cause of death.

According to the WHO, schistosomiasis affects 210 million people worldwide as of 2012. The disease is most commonly found in Africa, Asia, and South America, with around 700 million people in more than 70 countries living in areas where the disease is endemic. This makes it the most common parasitic infection after malaria and is second to malaria in terms of economic impact. In many endemic areas, schistosomiasis infects a large proportion of children under 14 years of age, so it produces a huge disability-adjusted life year (DALY). The WHO estimates that up to 200,000 people die as a direct result of liver complications associated with schistosomiasis each year and another 20 million suffer from complications, including portal hypertension, bleeding, severe anemia, and malnutrition. It is the most deadly of the neglected tropical diseases according to both the CDC and WHO. Of the nearly 800,000 cases of lethal cirrhosis world wide, nearly a quarter of the cases can be attributed to schistosomiasis (WHO estimate).

Experimental schistosomiasis is one of the few models of liver cirrhosis that truly models the disease seen in humans. The mode of infection and disease course is similar in man and mice. The reviewer seems to imply our data are important only if the findings are applicable to all forms and causes of liver cirrhosis. This scenario seems unlikely as the underlying etiologies and mechanisms of progressive liver disease in those etiologies are known to be diverse, including those observed in viral and parasitic infections, alcohol and drug toxicity, obesity, and autoimmune disorders. For example, a recent paper by Brenner, Kiseleva et al. showed that carbon tetrachloride (CCL4)-induced liver fibrosis is driven by an IL-17A-TGF-beta dependent mechanism (Meng, F. et al. IL-17 signaling in inflammatory Kupffer cells, hepatic stellate cells exacerbates liver fibrosis is mice. Gastroenterology. 2012). Therefore, it is unclear to us how additional studies with the CCL4 acute liver injury model will increase our understanding of the role of IL-13 and type 2 immunity in tissue regeneration and fibrosis. IL-13 is a well-accepted driver of fibrosis in many organ systems including the liver; therefore, we employed the very best model systems available to dissect its downstream mechanisms of action.

Two recent papers in Science and Nature emphasized the importance of better understanding the downstream targets of IL-13 signaling, so we feel our paper is both timely and exciting since it specifically investigates this important question. In the Nature and Science papers, the focus was on gut epithelium while our paper focuses on bile duct epithelium. Please refer to the recent commentary by Gronke and Diefenbach on these exciting papers:

(http://www.nature.com/icb/journal/v94/n3/full/icb201610a.html). In their commentary, they hypothesize that, "IL-13 may directly affect epithelial fate decisions". They write "an important avenue of future research (will be) to better flesh out how IL-13 affects signaling in epithelial cells and epithelial stem cells". These are the exact questions we explored in great detail in our study.

The BDL model mentioned by the reviewer is a commonly explored model of bile duct obstruction. This model also induces both fibrosis and bile duct reaction, so of the various artificial models the reviewer proposes we study, it is the only model that at least partly recapitulates the severe liver disease (steatosis, fibrosis, ductular reaction, and cholestasis) we see in schistosomiasis. However there is no existing literature suggesting that IL-13 plays a critical role in this experimental model of fibrosis. In the contrary, a recent study has attributed the pathology observed in BDL to upregulated TGF-B2 and IL-17 (Zepeda-Morales, A.S. et al.; 2016).

Taking into account the data from previously studies elucidating the mechanisms underlying the models proposed by the reviewer, we do not believe that repeating these studies will significantly add to this manuscript. However, we also must emphasize that this does not diminish the importance of the results we present for schistosomiasis, and the IL-13 pathway more specifically using IL-13 protein overexpression alone to recapitulate the pathologies observed during schistosomiasis. IL-13 has been identified as a key driver of pathology in a number of human diseases affecting multiple organ systems including idiopathic pulmonary fibrosis (IPF) (Chandriani et al., 2014; Murray et al., 2014), asthma (Choy et al., 2015; Scheerens et al., 2014), atopic dermatitis (Metwally et al., 2004), and ulcerative colitis (UC) (Heller et al., 2005), among others. Consequently, several clinical trials have been completed or are ongoing testing the safety and efficacy of modulating IL-13 levels in these various diseases (Beck et al., 2014; Brightling et al., 2015; Danese et al., 2015; Hamilton et al., 2014; Wenzel et al., 2013). In this context, we believe that our choice of models is both appropriate and timely, as it shows another instance of IL-13 directly driving fibrotic disease and associated pathology.

We have amended the text and have now cited previous human studies and ongoing clinical trials to make readily apparent the importance of IL-13 in driving pathology in diverse etiologies affecting many organs and to put our IL-13 overexpression studies into context.

Minor points

1. The statement that hydroxyproline measurement is more sensitive than picrosirius red staining is simply not correct.

Hydroxyproline accounts for approximately 23% of the amino acid content of collagen and is absent from nearly every other protein within the body (other proteins which contain hydroxyproline are produced in extremely low quantities and do not affect the outcome of the assay). Colorimetric quantitation of hydroxyproline gives a precise and highly linear estimate of the collagen content of a tissue and is sensitive and accurate over a 2^{11} scale (R^2 = 0.9998). Picrosirius red staining (PSR) is not collagen specific when viewed under brightfield and is only specific for collagen when viewed under circularly polarized light, resulting in a black background with green, red, or yellowish collagen fibrils which vary in color and intensity based upon several variables including the type of collagen, density, and 3D organization. While PSR quantitation is possible, it almost always fails to reliably account for density of collagen deposition, which can have profound consequences on the pathogenesis of hepatic disease such as driving portal-hypertension and subsequent esophageal varices, a significant cause of mortality. PSR can accurately assess the morphology of fibrosis, such as septal, peri-portal, centrilobal, sinusoidal etc., and can highlight these differences, which hydroxyproline quantitation would miss. Thus, these two methods combined provide a robust assessment of both the total collagen content of the liver and the morphological distribution of those collagens. We do not believe that any disagreement on these points changes any of the conclusions reached within this work and have amended the text accordingly

2. Original sources of mice should be properly cited (this applies to both the PDGFRB-Cre and the K19-CreERT mice as they were not generated by Dr. Forbes or Dr. Henderson; proper citation is important to acknowledge this important work).

We apologize for this omission and have added the appropriate citations to the methods to properly acknowledge the original generator of the lines.

3. More a comment than a formal criticism. The >95% recombination efficiency by K19-CreERT in Fig.S3 seems very unlikely.

The generally used protocol of 3 x 4mg doses of tamoxifen administered IP over the course of a week results in suboptimal recombination (~50% +/- 20% depending on the various studies analyzed and exact dosing regimen). The tamoxifen diet we utilized in our studies is estimated at 2.4 mg tamoxifen daily intake for a 30 g mouse. We administered this diet three weeks prior to beginning experiments and continued throughout the course (1 week for plasmid studies, 12 weeks for *S. mansoni* studies). Although not directly assessed, since the mice are continually being dosed with tamoxifen, we presume that their plasma levels of tamoxifen remain stable for longer periods of time, increasing the likelihood of recombination. Given these facts and our observations of stark and highly significant phenotypes in the K19-CreERT mice, we do not find it surprising that we observe robust recombination in our mice and believe that these findings are indeed accurate.

Meng, F.L., Wang, K., Aoyama, T., Grivennikov, S.I., Paik, Y., Scholten, D., Cong, M., Iwaisako, K., Liu, X., Zhang, M.J., *et al.* (2012). Interleukin-17 Signaling in Inflammatory, Kupffer Cells, and Hepatic Stellate Cells Exacerbates Liver Fibrosis in Mice. Gastroenterology *143*, 765-+.

Zaiss, A.K., Liu, Q., Bowen, G.P., Wong, N.C., Bartlett, J.S., and Muruve, D.A. (2002). Differential activation of innate immune responses by adenovirus and adeno-associated virus vectors. Journal of virology *76*, 4580-4590.

Zepeda-Morales, A.S., Del Toro-Arreola, S., Garcia-Benavides, L., Bastidas-Ramirez, B.E., Fafutis-Morris, M., Pereira-Suarez, A.L., and Bueno-Topete, M.R. (2016). Liver fibrosis in bile duct-ligated rats correlates with increased hepatic IL-17 and TGF-beta2 expression. Annals of hepatology *15*, 418-426.

Sincerely yours,

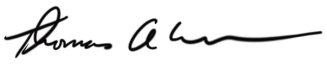

Thomas A. Wynn
Senior Investigator NIH/NIAID
4 Memorial Dr
Bethesda, MD 20892-0425, USA
Ph: 301-496-4758
twynn@niaid.nih.gov

Title: IL-13 activates distinct cellular pathways leading to ductular reaction, steatosis, and fibrosis

Authors: Richard L. Gieseck III[1, 2], Thirumalai R. Ramalingam[1], Kevin M. Hart[1], Kevin M. Vannella[1], David A. Cantu[1], Wei-Yu Lu[3], Sofía Ferreira-González[3], Stuart J. Forbes[3], Ludovic Vallier[2, 4], & Thomas A. Wynn[1,*]

Affiliations:

[1]Immunopathogenesis Section, Laboratory of Parasitic Diseases, National Institute of Allergy and Infectious Diseases, National Institutes of Health, Bethesda, Maryland, 20852, USA

[2]Wellcome Trust–Medical Research Council Stem Cell Institute, Anne McLaren Laboratory, Department of Surgery, University of Cambridge, Cambridge, UK

[3]Medical Research Council Centre for Regenerative Medicine, University of Edinburgh, Edinburgh, UK

[4]Wellcome Trust Sanger Institute, Hinxton, UK

Contact:

[*]Corresponding Author: twynn@niaid.nih.gov

Summary:

Fibroproliferative diseases are driven by dysregulated tissue repair responses and are a major cause of morbidity and mortality as they affect nearly every organ system in the body. Type-2 cytokine responses (interleukin-4 and interleukin-13) are critically involved in tissue repair; however, the mechanisms that regulate repair versus pathological fibrosis are not well understood. Here, we show that the type-2 effector cytokine interleukin-13 simultaneously, yet independently, directs hepatic fibrosis and the compensatory proliferation of hepatocytes and biliary cells in progressive models of liver disease induced by IL-13 over-expression or

following infection with *Schistosoma mansoni*. Using conditional mutant mice with interleukin-13 signaling genetically disrupted in hepatocytes, cholangiocytes, or resident tissue fibroblasts, we reveal direct and distinct roles for interleukin-13 in fibrosis, steatosis, cholestasis, and ductular reaction. Together, these studies show that these mechanisms are simultaneously controlled but distinctly regulated by interleukin-13 signaling. Thus, it may be possible to promote IL-13-dependent hepatobiliary expansion without generating pathological fibrosis.

Highlights and eTOC Blurb:

- Type-2 fibrosis and regeneration are directly but independently mediated by IL-13
- Pathological fibrosis is driven by direct IL-13 signaling in PDGFRB^{+} fibroblasts
- IL-13 stimulates hepatobiliary progenitor cells and cholangiocytes to proliferate
- IL-13 regulates lipogenesis, bile acid synthesis, and biliary-dependent steatosis

Fibroproliferative diseases will affect nearly half of the global population and result in significant loss in quality of life. In this work, we demonstrate that the type-2 cytokine interleukin-13 signals through distinct cellular pathways to simultaneously drive hepatic fibrosis, steatosis, cholestasis, and hepatobiliary proliferation. The insights gained from this work demonstrating the possibility of decoupling IL-13-driven regenerative processes from tissue fibrosis may be instrumental in developing novel cell-targeted therapies exploiting these specific pathways for therapeutic benefit.

Introduction:

The liver is remarkable in its ability to regenerate despite repeated injury. Different from many other organs which utilize stem cell populations in order to replace tissues, the liver relies heavily upon hepatocytes and cholangiocytes to exit quiescence and divide (Yanger et al., 2014). Recent studies have demonstrated distinct hepatocyte subsets, which contribute to hepatocyte turnover during homeostasis (Wang et al., 2015) and during mild chronic injury (Font-Burgada et al., 2015). However, during severe chronic injury, damaged hepatocytes can lose the ability to

divide (Roskams, 2006), and in response, a population of putative hepatobiliary progenitor cells (HPCs) expands (Farber, 1956; Huch et al., 2015; Lu et al., 2015). Although several studies have questioned the source of HPCs and whether HPCs exhibit bipotent progenitor capacity (Jors et al., 2015), other recent studies have demonstrated that these cells can completely repopulate the liver following injuries that induce hepatocellular senescence (Lu et al., 2015). These differences in behavior and potency of HPCs may be explained by differences in the etiology of liver injury; nevertheless, it has been well established that the dysregulated signaling microenvironment of the injured liver can lead to aberrant proliferation of both HPCs and existing cholangiocytes, together facilitating a disorganized expansion of bile ducts and recruitment of inflammatory cells known as ductular reaction (DR) (Roskams et al., 2004).

Ductular reactions are encountered in virtually every acute and chronic liver disorder in which there is organ-wide liver damage and cell loss. Proliferating ductules derived from HPCs or existing cholangiocytes may fail to drain bile contents properly, leading to local necrosis and progression towards cancers such as hepatocellular or cholangiocarcinoma (Alison and Lovell, 2005; Park et al., 2007). Furthermore, it has been well documented that the presence of these proliferating cells is highly correlated with the progression of hepatic fibrosis and emergence of lipid abnormalities, although the detailed mechanisms behind these correlations are debated and not well understood (Clouston et al., 2005; Richardson et al., 2007). Thus, presence of DRs is an important prognostic marker of advanced liver disease, with patients exhibiting DRs generally having poorer clinical outcomes (Lowes et al., 1999; Roskams, 2006; Sancho-Bru et al., 2012). Nevertheless, the signaling pathways governing these dysregulated responses remain unclear, limiting our ability to combat these severe complications in the clinic.

Interleukin-13 (IL-13) has been identified as a major pathogenic cytokine in helminth induced liver disease and several other chronic diseases associated with persistent type-2 cytokine production (Chiaramonte et al., 1999). Consequently, therapeutic antibodies targeting IL-13 signaling pathways are currently being investigated in several major clinical trials. Interestingly however, type-2 cytokine responses have also been linked with wound repair following acute tissue injury (Chen et al., 2012; Kaviratne et al., 2004). Nevertheless, the mechanisms that govern tissue regeneration versus pathological type-2-driven fibrosis remain unclear. While previous studies have implicated M2 macrophages in repair and fibrosis (Borthwick et al., 2015; Chen et al., 2012), other cells including hepatocytes, cholangiocytes,

HPCs, and fibroblasts also express functional IL-4/IL-13 receptors, yet their roles in the progression of liver disease, steatosis, fibrosis, DR, and liver regeneration during chronic type-2 cytokine-driven inflammatory responses have remained unclear. Moreover, while clinical studies have found elevated type-2 cytokines and receptor expression in human patients with biliary atresia (Li et al., 2011), primary biliary cirrhosis, primary sclerosing cholangitis, hepatitis C infection, and autoimmune hepatitis (Landi et al., 2014), no previous studies have directly investigated the correlative and causal relationships between type-2-driven fibrosis and DR. Therefore, we generated a series of cell-specific knockout mice in which the IL-4 receptor alpha chain (IL4Rα), an essential receptor component for both IL-4 and IL-13 signaling, was targeted for deletion in biliary cells (defined as both HPCs and existing cholangiocytes), hepatocytes, and fibroblasts in order to elucidate the cellular pathways instructed by IL-13 that regulate the emergence of ductular reactions and fibrosis during schistosomiasis, a disease affecting over 300 million individuals that induces a progressive liver fibrosis that manifests many of the complications seen in advanced cirrhosis of many etiologies.

Results:

IL-4/13 Signaling in Hepatocytes and/or Biliary Cells drives DR but not Fibrosis

IL4Rα$^{flox/flox}$Albumin$^{WT/Cre}$ (Alb-Cre^{+}) mice and IL4Rα$^{flox/flox}$ (Alb-Cre^{-}) littermates were studied over the course of an 18-week *S. mansoni* infection that results in progressive, type-2-driven liver fibrosis. Due to expression of albumin by hepatoblasts (Sparks et al., 2010), the developmental precursor of both hepatocytes and cholangiocytes, these mice express cre-recombinase in both the hepatocyte and biliary compartments, and therefore have impaired IL4Rα expression in both hepatocytes and biliary cells. No significant differences in fibrosis were seen at 10 or 18 weeks as assessed by tissue hydroxyproline levels (Figure 1A) and picrosirius red (PSR) staining (Figure 1B), ruling out a role for IL-4/IL-13 signaling through IL4Rα-expressing hepatocytes, cholangiocytes, or HPCs in the progression of fibrosis. Epithelial cell adhesion molecule (EpCAM) uniquely marks the biliary compartment and cells recently derived from HPCs within the liver (Yoon et al., 2011), and by 10 weeks post-infection, marked expansion of EpCAM^{+} cells was evident around the granulomas of Alb-Cre^{-} mice but was significantly less in the Alb-Cre^{+} group (6.0 ± 1.3% EpCAM^{+} vs. 2.3 ± 0.4% EpCAM^{+}, $p <$

0.01; Figure 1C upper panels, D). By 18 weeks, Alb-Cre$^-$ mice exhibited abundant EpCAM$^+$ ductules in the periphery of the granulomas, but the Alb-Cre$^+$ group did not (19.5 ± 4.3% EpCAM$^+$ vs. 3.8 ± 0.5% EpCAM$^+$, $p < 0.001$; Figure 1C lower panels, D,). Additionally, Alb-Cre$^-$ mice exhibited significantly elevated liver weights compared to their Alb-Cre$^+$ littermates (Figure 1E) in agreement with a recent study implicating IL-4 signaling with hepatocyte proliferation (Goh et al., 2013). Nearly 36% of EpCAM$^+$ cells in Alb-Cre$^-$ mice co-stained positive for Ki-67 indicating active proliferation in response to IL-13, while only 2% of those in Alb-Cre$^+$ littermates were actively proliferating (Figure 1F, H). Alb-Cre$^-$ mice also exhibited spotty microvesicular steatosis as assessed by Oil Red O staining (ORO) in hepatocytes throughout the liver (Figure 1I), which was visually diminished in the Alb-Cre$^+$ group. No significant differences were seen in serum ALT and AST levels (Figure 1G), survival (Figure S1A), and worm burden (Figure S1B), suggesting that differences in liver injury severity were not contributing to these changes. Together, these data unequivocally demonstrate that IL-4/IL-13 signaling through hepatocytes and/or biliary cells is necessary for the DR and steatosis associated with *S. mansoni* infection, but does not significantly affect fibrosis (Figure 1J).

IL-13 but not IL-4 is Necessary for DR during S. mansoni Infection

IL4Rα is implicated in two distinct signaling pathways (Ramalingam et al., 2008). Type-I signaling is mediated solely by IL-4 following engagement of IL4Rα:γ_c heterodimers by IL-4. Whereas type-II signaling is activated when either IL-4 or IL-13 engage IL4Rα:IL13Rα1 heterodimers. In order to determine if the DR seen in Alb-Cre$^-$ but not in Alb-Cre$^+$ littermates (Figure 2A, B, F) is mediated through type-I or type-II IL4Rα signaling, we utilized an IL13Rα1$^{-/-}$ model in order to selectively deplete type-II signaling. After 12 weeks of infection, no evidence of DR was seen, suggesting that type-II signaling is necessary for the development of *S. mansoni* driven ductular response (Figure 2C, F). Given that both IL-4 and IL-13 can signal through the type-II IL4Rα signaling complex, we set out to determine if one of these cytokines plays a dominant role in the progression of DR or if either is sufficient. To this end, we utilized IL-4$^{-/-}$ and IL-13$^{-/-}$ mice to look for the presence of DR after the course of a 12-week infection. IL-4$^{-/-}$ mice developed DR similar to wild type controls (Figure 2D, F); however, DR in IL-13$^{-/-}$ mice

was absent (Figure 2E, F), suggesting that IL-13 is the dominant type-2 cytokine in the progression of *S. mansoni* mediated DR (Figure 2G).

IL-13 Signaling in Hepatocytes and/or Biliary Cells Induces DR and Steatosis, but not Fibrosis

IL-13 has been identified as a key driver of pathology in a number of human diseases affecting multiple organ systems including idiopathic pulmonary fibrosis (IPF) (Chandriani et al., 2014; Murray et al., 2014), asthma (Choy et al., 2015; Scheerens et al., 2014), atopic dermatitis (Metwally et al., 2004), and ulcerative colitis (UC) (Heller et al., 2005), among others. Consequently, several clinical trials have been completed or are underway testing the safety and efficacy of modulating IL-13 levels in these diseases (Beck et al., 2014; Brightling et al., 2015; Danese et al., 2015; Hamilton et al., 2014; Wenzel et al., 2013). In the previous section, we showed that DR requires direct IL-13 signaling on hepatobiliary cells during the course of *S. mansoni* infection; however, helminth infections result in a complex immune response and an intercellular signaling environment that evolves over time (Pearce and MacDonald, 2002). In order to determine the specific role of IL-13 directly and in the absence of other etiological agents, we designed an IL-13 overexpression plasmid (13-OP) and used hydrodynamic tail vein injection in order to induce overexpression within the liver (Liu et al., 1999). Quantitation of mRNA collected from liver 9 days post injection determined that 13-OP caused a significant upregulation of IL-13 mRNA and specific STAT6-inducible targets such as procollagen 6a (Col6a1) and interleukin-13 receptor alpha 2 (IL13Rα2) without inducing an IL-4 response (Figure 3A). 13-OP induced a significant fibrotic response in both the Alb-Cre$^+$ and Alb-Cre$^-$ groups as assessed by tissue hydroxyproline content (Figure 3B) and PSR staining (Figure 3C), again ruling out a role for IL-13 signaling through IL4Rα-expressing hepatocytes, cholangiocytes, or HPCs in the progression of fibrosis. Here again, EpCAM$^+$ ductules in Alb-Cre$^-$ mice were Ki-67$^+$ (over 39%), indicating that they were actively proliferating, while little evidence of proliferation was observed in the Alb-Cre$^+$ mice (under 1.8% Ki-67$^+$, Figure 3D, G). Strikingly, 13-OP also induced significant steatosis in the Alb-Cre$^-$ mice but not in the Alb-Cre$^+$ group (7.2 ± 0.8% ORO$^+$ vs 0.04% ± 0.01% ORO$^+$, $p < 0.0001$; Figure 3E, H) that corresponded with increases in serum triglyceride levels in the Alb-Cre$^-$ group (Figure 3F). No significant differences were seen in survival (Supplementary Figure 2A) or serum ALT and AST levels

(Supplementary Figure 2b), once again suggesting that differences in injury severity are not underlying these changes.

Microarray analyses were performed on whole liver from the 13-OP mice and GFP-OP control groups to elucidate the signaling pathways being activated by IL-13 signaling in hepatocytes and biliary cells. Over 130 genes exhibited over a two-fold difference ($p < 0.01$) between the 13-OP Alb-Cre^{+} and Alb-Cre^{-} groups (Figure 3I). Key differences include the downregulation of the classical and acidic pathways of bile acid synthesis, induction of cellular senescence, metabolic switch to lipogenesis, and recruitment of type-2 immune mediators (Figure 3J, L), all of which were dependent on IL-13 signaling through IL4Rα^{+} hepatocytes/biliary cells. Furthermore, Ingenuity Pathway Analysis (IPA) revealed the key mediators induced by IL-13 signaling in Alb-Cre^{-} mice that were not active in Alb-Cre^{+} littermates (Figure 3K). These data establish that IL-13 protein alone can directly recapitulate key aspects of *S. mansoni*-driven pathology including fibrosis, ductular proliferation, and steatosis. Furthermore, mice with non-functional IL4Rα in hepatocytes and biliary cells display markedly reduced ductular proliferation and steatosis but develop normal fibrosis, confirming the critical role of IL-13 and IL4Rα signaling in these cell types for development of DR and steatosis, further supporting the growing data demonstrating IL-13 as a key pathogenic agent in a variety of human diseases affecting many organ systems.

Direct IL-13 Signaling in Biliary Cells Induces DR and Steatosis, but not Fibrosis

Since the Alb-Cre model induces recombination in both the hepatocyte and biliary compartments, we next utilized an IL4Rα$^{flox/flox}$Keratin19$^{WT/CreERT}$ model in order to restrict recombination to the adult biliary compartment (Means et al., 2008), allowing us to discern the distinct role of type-2 signaling in biliary cells. IL4Rα$^{flox/flox}$K19$^{WT/CreERT}$ (K19-Cre^{+}) and IL4Rα$^{flox/flox}$ (K19-Cre^{-}) littermates were administered tamoxifen diet for 3 weeks prior to 13-OP injection to induce deletion of the IL4Rα-floxed segments in cholangiocytes and HPCs, but not hepatocytes. This administration regimen resulted in specific recombination in 95.1 ± 2.6% of EpCAM^{+} cells (Figure S3A, B). After 1 week, 13-OP induced a significant fibrotic response in both the K19-Cre^{+} and K19-Cre^{-} groups as evaluated by tissue hydroxyproline content (Figure 4A), PSR staining (Figure 4B), and mRNA quantitation (Figure 4C), mirroring the results

obtained with the Alb-Cre expressing mice. $EpCAM^+$ ductules in $K19\text{-}Cre^-$ mice, but not $K19\text{-}Cre^+$, co-stained positive for Ki-67 expression (30.8 ± 4.6% vs. 5.8 ± 1.4%, $p < 0.0001$), illustrating a direct and critical role for IL-13-IL4Rα signaling in biliary cell proliferation (Figure 4D, E). Additionally, 13-OP induced severe steatosis in the $K19\text{-}Cre^-$ mice but not the $K19\text{-}Cre^+$ mice (6.4 ± 0.5% ORO^+ vs 0.07 ± 0.05% ORO^+, $p < 0.0001$), suggesting that the upstream initiator of the steatosis seen in the $Alb\text{-}Cre^-$ and $K19\text{-}Cre^-$ mice is IL-13 signaling through the biliary compartment rather than through hepatocytes (Figure 4F, G). No significant differences were seen in survival (Figure S4A) and serum ALT and AST levels (Figure S4B) once again suggesting that differences in injury severity were not responsible for these changes.

To verify these results in an infectious setting, we subjected the K19-Cre mice to a 12-week *S. mansoni* infection. Mice were administered tamoxifen diet the entire course of infection to induce recombination. Similar to results from previous experiments using the Alb-Cre models and the K19-Cre 13-OP model, no significant differences in hydroxyproline content or picrosirius red staining were observed between the two infected groups (Figure 4I, J). In contrast to the Alb-Cre model, in which hepatocyte IL-4/13 signaling was disrupted, no differences in liver weight were observed between groups, again supporting previous work that has suggested that IL-4/13 acts directly on hepatocytes as a hepatocyte mitogen during injury (Goh et al., 2013) (Figure 4K). Similar to the other models, $EpCAM^+$ ductules in $K19\text{-}Cre^-$ mice, but not $K19\text{-}Cre^+$, co-stained positive for Ki-67 expression (27.8 ± 9.0% vs. 5.8 ± 1.2%, $p < 0.05$; Figure 4M, N). No significant differences in infection burden or serum ALT and AST were observed, ruling out that differences in ductular reaction are simply due to underlying differences in injury severity (Figure 4L, O). These data clearly establish that IL-13 signaling in biliary cells, not hepatocytes, results in ductular proliferation and steatosis without affecting fibrosis (Figure 4H).

Since the K19-Cre targets both cholangiocytes and HPCs in the adult liver, we next explored whether IL-13 could directly stimulate isolated HPCs. $CD45^-$ $CD31^-$ $TER119^-$ $EpCAM^+$ $CD24^+$ $CD133^+$ HPCs (Lu et al., 2015) were isolated from the livers of $IL4R\alpha^{flox/flox}$ mice and stimulated with 50 ng/mL recombinant murine IL-13 or a vehicle control for 72 hours. IL-13 treatment caused cells to adopt a more cuboidal shape with clearly defined cell boundaries (Figure S5A). Additionally, IL-13 treated cells proliferated more quickly than controls as assessed by Alamar blue reduction (Figure S5B). We employed microarray analysis to determine

the pathways driven by IL-13 to establish the observed phenotype. More than 200 genes exhibited over a 1.5-fold difference between the control and IL-13 treated groups (Figure S5C) including genes involved in Wnt and Notch signaling, key pathways in cholangiocyte differentiation, as well as immune cell trafficking and recruitment (Figure S5D). Taken together, these data suggest that IL-13 directs isolated HPCs towards a cholangiocyte fate and recruits cells that have been shown to further contribute to cholangiocyte differentiation.

IL-13 Signaling through PDGFRB^{+} Fibroblasts is Necessary for Type-2 Fibrosis

Next, in order to address the question of whether IL-13 signaling through fibroblasts is necessary for type-2-driven fibrosis and/or ductular proliferation, we utilized an IL4Rα$^{flox/flox}$PDGFRB$^{WT/Cre}$ (PDGFRB-Cre^{+}) model to disrupt IL-13 signaling specifically in liver resident tissue fibroblasts, also known as hepatic stellate cells (HSCs). Previous work has demonstrated that within the liver, the PDGFRB-Cre induces recombination specifically in HSCs and not in endothelium, macrophages, hepatocytes, cholangiocytes, or T cells (Henderson et al., 2013). Furthermore, we isolated HSCs from wild type and PDGFRB-Cre^{+} mice and looked for the presence of native or recombined IL4Rα by genomic DNA genotyping and found efficiency of recombination approaching 100% (Figure S11). We subjected these mice to 13-OP and GFP-OP injections and followed them for 7 days. PDGFRB-Cre^{+} mice were significantly protected from fibrosis as assessed by tissue hydroxyproline content (Figure 5A) and PSR staining (Figure 5B), providing the first direct evidence that IL-13 signaling in PDGFRB^{+} fibroblasts *in vivo* is critical for the development of fibrosis. mRNA expression showed significant upregulation of the fibrosis related transcripts procollagen 6a and periostin in the PDGFRB-Cre^{-} group compared to PDGFRB-Cre^{+} littermates (Figure 5C). Furthermore, PDGFRB-Cre^{+} mice were significantly protected from mortality (Figure S6A). Both groups exhibited marked microvesicular steatosis after 13-OP administration (Figure 5D). Despite the marked decrease in fibrosis and increased survival in the PDGFRB-Cre^{+} mice, both 13-OP groups exhibited EpCAM^{+}Ki-67^{+} ductular reaction (36.1 ± 10.5% vs. 27.0 ± 4.5%, $p > 0.05$; Figure 5E, Figure S7A), further illustrating that ductular reaction and fibrosis are distinctly and independently regulated by IL-13.

In order to validate these results in a chronic disease setting, in a final series of studies, PDGFRB-Cre mice were infected with *S. mansoni* and followed for twelve weeks. PDGFRB-

Cre^+ mice were markedly protected from the development of fibrosis as quantified by tissue hydroxyproline content (Figure 5F) and visualized by PSR staining (Figure 5G). Despite the significant differences in fibrosis, no significant differences were seen in survival at least through week 12 post-infection (Figure S6B). Quantitation of mRNA expression by qPCR revealed a stronger type-2 effector response in the PDGFRB-Cre^+ mice, likely due to the decreased expression of the neutralizing decoy receptor IL13Rα2 by $PDGFRB^+$ fibroblasts (Figure S8). Despite the significant decrease in fibrosis in the PDGFRB-Cre^+ mice, both groups exhibited extensive ductular proliferation in the periphery of granulomas that co-stained $EpCAM^+Ki\text{-}67^+$ (27.3 ± 6.4% vs. 27.4 ± 6.7%, $p > 0.05$; Figure 5H, Figure S7B), clearly demonstrating that fibrosis and ductular proliferation are independently regulated by IL-13 signaling through distinct cell types.

IL-13 Signaling in Hepatocytes and Fibroblasts Assists in the Recruitment of Eosinophils

Previous studies have identified eosinophils as a local source of IL-13 during chronic liver injury (Reiman et al., 2006). In this study, we observed a significant role for hepatocytes and $PDGFRB^+$ fibroblasts in eotaxin-1 expression and the recruitment of eosinophils to the liver following type-2-driven injury (Figure 6A-C). Although the results with K19-Cre^+ mice revealed that IL4Rα-expressing biliary cells have no significant role in eotaxin-1 expression or eosinophil recruitment, the close proximity of $PDGFRB^+$ periportal fibroblasts likely contributed to the marked accumulation eosinophils in areas surrounding bile ducts. Consequently, in addition to ILC2s and Th2 cells, eosinophils recruited by IL4Ra-expressing hepatocytes and fibroblasts likely serve as local sources of IL-13, which reinforce myofibroblast activation and ductular proliferation following injury (Figure 6D). As such, these findings reveal a previously unknown link between hepatocytes, fibroblasts, and eosinophils in the development of both fibrosis and ductular reactions and represent a new pathway contributing to these pathologies in the liver.

IL-13 Driven DR Initiates Ductal Cholestasis Independently from Fibrosis

Cholestatic complications are a common feature of chronic fibrotic liver diseases and can result in local necrosis and progression towards cancers such as hepatocellular or

cholangiocarcinoma (Alison and Lovell, 2005; Park et al., 2007). Despite this, it is unknown whether cholestasis originates from physical stricture of bile ducts (obstructive cholestasis) or from other distinct mechanisms during the progression of IL-13-dependent fibrosis. In our various models of type-2-driven liver damage, cholestasis was observed in the large branching ducts of Cre- groups from each experiment, all of which exhibited both extensive fibrosis and ductular proliferation (Figure 7A, B, C). Alb-Cre^{+} and K19-Cre^{+} mice, in which ductular proliferation was eliminated but fibrosis was maintained, showed little evidence of cholesterol crystal precipitation, suggesting that excessive ductular proliferation, rather than fibrosis, initiates cholestasis in response to IL-13 (Figure 7A, B). This hypothesis was further supported by the observation that PDGFRB-Cre^{+} mice, in which fibrosis is reduced to levels of naïve animals but ductular proliferation proceeds unimpeded, exhibited marked ductal cholestasis, as evidenced by the precipitation of cholesterol crystals in the large branching ducts (Figure 7C). Furthermore, in all mice exhibiting DR, many bile ducts had proliferated to the point of occluding the bile duct lumen (Figure 7D). Resin casting of the biliary tree in mice over-expressing IL-13 confirmed that these mice have strictures, presumably induced by excessive proliferation that results in a truncated biliary tree with many proliferative nodules, further supporting our hypothesis that excessive ductal proliferation rather than fibrosis results in cholestatic precipitation and injury (Figure 7E, F). These discoveries emphasize that strategies utilizing type-2 cytokine driven repair and regeneration will need to be finely tuned and targeted to prevent these potentially serious complications.

Discussion:

Some studies have suggested that IL-13 promotes fibrosis by increasing autocrine CTGF signaling in fibroblasts and by inducing expression of the pro-fibrotic cytokine TGF-β1 via IL-13Rα2 signaling (Liu et al., 2011; Shimamura et al., 2008; Sugimoto et al., 2005). However, studies with neutralizing anti-TGF-β antibodies, soluble antagonists (soluble TGF-βR-Fc), and Tg mice (Smad3$^{-/-}$ and TGF-βRII-Fc), have suggested that IL-13 can also induce fibrosis independently from TGF-β. IL13Rα2$^{-/-}$ mice were also found to develop significantly worse IL-13 driven fibrosis than wild type littermates, shedding further doubt on the importance of IL13Rα2 triggered TGF-β1 expression (Chiaramonte et al., 2003). Instead, related studies have

argued for a direct and critical role for IL4Rα-IL13Rα1 triggered STAT6-signaling in the development of type-2 cytokine driven fibrosis (Wynn, 2015). However, whether IL-13 driven fibrosis is induced by direct targeting of fibroblasts *in vivo* or by other intermediate cell types and signaling mechanisms has remained unknown until this study. Here, we provide unequivocal evidence that IL-13 must engage fibroblasts directly to promote fibrosis and that disruption of this signaling pathway in $PDGFRB^{+}$ HSCs is sufficient to reduce fibrosis to levels found in naïve animals. Furthermore, these studies establish that ductular reaction is completely uncoupled from fibrosis. During chronic type-2 driven injury, circulating IL-13 directly targets both fibroblasts and biliary cells, resulting in the activation of ECM-producing myofibroblasts and concurrent ductular reaction (Figure 5I), thus finally resolving the enigmatic correlation between ductular reactions and fibrosis.

Together, these studies have revealed the distinct cell types targeted by IL-13 that concurrently drive hepatobiliary fibrosis, proliferation, steatosis, and associated pathologies (Figure 5I). The duration and magnitude of the IL-13 response likely dictates whether the resulting repair response is adaptive or maladaptive. For example, in schistosomiasis, the fibrotic response initially encapsulates parasite eggs to prevent hepatocyte damage from cytotoxic egg antigens; however, during chronic infection, excessive accumulation of extracellular matrix components ultimately impedes blood flow, thus exacerbating damage.

Similarly, we have shown that IL-13 can act directly on cholangiocytes *in vivo* (Figure 4) and promote HPC differentiation towards a cholangiocyte fate *in vitro* (Figure S5). We hypothesize that IL-13, a known angiogenic factor (Fukushi et al., 2000) that regulates neovascularization, also evolved to target HPCs and cholangiocytes to promote ductular repair following injury. During acute hepatic injury, local sources of IL-13 from cell types such as ILC2s may assist in regeneration by prompting a transient proliferation of cholangiocytes to replace damaged ducts. However, in chronic cases where tissue-damaging irritants cannot be cleared, or during adaptive Th2-driven immune responses such as those present during chronic parasitic diseases, ductular proliferation can become maladaptive, predisposing to cholestatic complications as evidenced by the rapid occlusion of bile ducts and precipitation of cholesterol crystals within the large branching ducts (Figure 7).

The fact that steatosis was not seen in Alb-Cre$^+$ and K19-Cre$^+$ mice (Figures 1I, 3H, and 4G), which have impaired ductular proliferation but normal fibrosis, but was present in PDGFRB-Cre$^+$ mice (Figure 5D), which have extensive ductular proliferation yet minimal fibrosis, supports the conclusion that steatosis is caused by IL-13-driven ductular occlusion rather than a result of severe fibrotic complications and fibrosis-driven ductal stricture. Furthermore, since steatosis failed to develop in both Alb-Cre$^+$ (impaired IL-13 signaling through hepatocytes) and K19-Cre$^+$ mice (normal IL-13 signaling in hepatocytes), one can rule out that cholestatic steatosis is induced by metabolic changes due to IL-13/STAT6 (Ricardo-Gonzalez et al., 2010) or IL-13/STAT3 (Stanya et al., 2013) signaling in hepatocytes as has been suggested previously. Instead, we posit that malabsorbtion of fat, due to lack of bile flow to the intestine secondary to IL-13 driven ductal occlusion, results in the induction of a lipogenic program (Figure 3J) within hepatocytes in order to compensate for lack of dietary fat, resulting in the steatotic appearance of hepatocytes in mice with ductular reaction. These findings are consistent with the steatosis that develops in rats during experimental bile duct ligation (Lin et al., 2011) and in human patients with extrahepatic cholestasis (Schaap et al., 2009). Indeed, our mice developed decreased glucokinase, decreased CYP7A1, increased FGF21, decreased glucose, and increased triglycerides (Figure 3), features commonly observed in patients with extrahepatic cholestasis.

We further hypothesize that the downregulation of the bile acid biosynthesis pathway (Figure 3I-L) may be part of a previously unappreciated feedback loop to mitigate the cholestatic damage ensuing from counterproductive ductular proliferation. Surprisingly, we find no evidence of hepatocytic cholestasis (Figure S9) despite the fact that we have ample evidence of obstructive cholestasis, likely due to this downregulation of bile acid synthesis secondary to bile duct occlusion. These data likely explain the previously underappreciated link between ductular and lipid abnormalities that has been noted in patients with primary biliary cirrhosis (Sorrentino et al., 2010) and warrant further detailed investigation into the metabolic changes induced by IL-13-driven ductular proliferation in the context of chronic fibrosis.

In summary, we have shown that IL-13 simultaneously, yet independently, directs fibrosis and hepatobiliary proliferation in both an infection induced and a sterile model of liver fibrosis. Surprisingly, both mechanisms appear to operate independently of IL-33 (Figure S10), which was recently found to promote extrahepatic, but not intrahepatic, ductal proliferation in

experimental biliary atresia (Li et al., 2014). These IL-13-driven pathways likely represent an evolutionary response to preserve liver function during the course of chronic inflammatory liver disease. Nevertheless, during a relentless type-2-driven disease, these regenerative responses quickly evolve into maladaptive processes as fibrosis and ductular reactions accrue, and the associated steatosis and cholestasis worsen. It has been noted that between 80-90% of liver transplants experience major bile duct epithelium loss during the procedure, resulting in serious complications in up to 40% of patients (Karimian et al., 2013). Thus, these findings are of significant interest to clinical and translational medicine because they reveal the potential therapeutic and biomarker potential of IL-13 signaling in cholangiocyte differentiation and biliary regeneration. Particularly, we believe the insights gained from this work demonstrating the possibility of decoupling the IL-13-driven proliferative processes from tissue fibrosis will be instrumental in developing novel cell-targeted therapies exploiting these specific pathways.

Experimental Procedures:

Ethics Statement

The National Institute of Allergy and Infectious Diseases Division of Intramural Research Animal Care and Use Program, as part of the National Institutes of Health Intramural Research Program, approved all of the experimental procedures (protocol LPD 16E). The Program complies with all applicable provisions of the Animal Welfare Act (http://www.aphis.usda.gov/animal_welfare /downloads/awa/awa.pdf) and other federal statutes and regulations relating to animals.

Mice

Alb-Cre: IL4Rα$^{flox/flox}$ mice were kindly provided by Dr. Frank Brombacher (University of Cape Town; Cape Town, South Africa). Alb$^{Cre/Cre}$ mice were purchased from Jackson Laboratories. IL4Rα$^{flox/flox}$ females were crossed with Alb$^{Cre/Cre}$ males to generate IL4Rα$^{WT/flox}$ Alb$^{WT/Cre}$ mice. IL4Rα$^{WT/flox}$Alb$^{WT/Cre}$ males were backcrossed to IL4Rα$^{flox/flox}$ females to generate IL4Rα$^{flox/flox}$Alb$^{WT/Cre}$ and IL4Rα$^{flox/flox}$Alb$^{WT/WT}$ progeny. IL4Rα$^{flox/flox}$Alb$^{WT/Cre}$ males

were continually backcrossed to IL4Rα$^{flox/flox}$ females. The resulting IL4Rα$^{flox/flox}$Alb$^{WT/Cre}$ and IL4Rα$^{flox/flox}$Alb$^{WT/WT}$ progeny were used for experiments.

K19-Cre: K19$^{CreERT/CreERT}$Rosa26$^{tdTomato/tdTomato}$ mice were kindly provided by Prof. Stuart Forbes (University of Edinburgh, Edinburgh, UK) and were generated by Dr. Guoqiang Gu (Means et al., 2008). IL4Rα$^{flox/flox}$ females were crossed with K19$^{CreERT/CreERT}$Rosa26$^{tdTomato/tdTomato}$ males to produce IL4Rα$^{flox/WT}$K19$^{WT/CreERT}$ Rosa26$^{WT/tdTomato}$ progeny. IL4Rα$^{flox/WT}$K19$^{WT/CreERT}$ Rosa26$^{WT/tdTomato}$ males were backcrossed to IL4Rα$^{flox/flox}$ females to produce IL4Rα$^{flox/flox}$K19$^{WT/CreERT}$Rosa26$^{WT/tdTomato}$ and IL4Rα$^{flox/flox}$K19$^{WT/WT}$ Rosa26$^{WT/tdTomato}$ offspring that were used for experiments.

PDGFRB-Cre: PDGFRB$^{Cre/Cre}$ mice were kindly provided by Dr. Neil Henderson (University of Edinburgh, Edinburgh, UK) and were generated by Dr. Ralf Adams (Foo et al., 2006). IL4Rα$^{flox/flox}$ females were crossed with PDGFRB$^{Cre/Cre}$ males to produce IL4Rα$^{flox/WT}$PDGFRB$^{Cre/WT}$ progeny. IL4Rα$^{flox/WT}$PDGFRB$^{Cre/WT}$ males were backcrossed to IL4Rα$^{flox/flox}$ females to produce IL4Rα$^{flox/flox}$PDGFRB$^{Cre/WT}$ and IL4Rα$^{flox/flox}$PDGF$^{WT/WT}$ offspring that were used for experiments.

Other mice: IL4$^{-/-}$ mice were kindly provided by Dr. William E. Paul (NIAID, NIH). IL13$^{-/-}$ mice were kindly provided from Dr. Andrew Mckenzie (MRC Laboratory of Molecular Biology). IL13Rα1$^{-/-}$ mice were kindly provided by Regeneron Pharmaceuticals Inc. (Tarrytown, NY). IL33$^{-/-}$ mice were kindly provided by Amgen Inc. (Seattle, WA).

All animals were housed under specific pathogen-free conditions at the National Institutes of Health in an American Association for the Accreditation of Laboratory Animal Care-approved facility. Experiments used littermates (both sexes) between 8-16 weeks of age unless otherwise noted.

S. Mansoni Infection

Mice were infected percutaneously by suspending tails in water containing 35 *Schistosoma mansoni* cercariae for 45 minutes. Cerceriae were obtained by shedding infected *Biomphalaria glabrata* snails (Biomedical Research Institute; Rockville, MD). At the time of

euthanasia, livers were perfused in order to determine worm burden and were removed for subsequent analyses.

Plasmid Overexpression

IL-13 and eGFP overexpression plasmids were produced by GenScript USA Inc. (Piscataway, NJ) by ligating the ORFs for IL-13 (NM_008355) and eGFP into the multi-restriction site of a pRG977 vector (kindly provided by Regeneron Pharmaceuticals Inc.). Hydrodynamic delivery was performed as described previously (Liu et al., 1999).

Blood Analysis

Blood was collected in Serum Gel Z/1.1 tubes (Sarstedt) and serum was separated by centrifuging for 5 minutes at 5,000g. Serum was analyzed for sodium, potassium, chloride, calcium, magnesium, phosphorus, glucose, BUN, creatinine, uric acid, albumin, total protein, cholesterol, triglycerides, alkaline phosphatase, AST, ALT, amylase, creatine kinase, and lactate dehydrogenase at the National Institutes of Health Clinical Center using a Vista Analyzer (Siemens; Deerfield, IL).

Histopathology

Liver tissue was fixed in Hollande's fixative overnight and subsequently washed with 70% ethanol. Tissue was then embedded in paraffin for sectioning and stained with Wright's Giemsa and picrosirius red (Histopath of America; Clinton, MD). Samples stained for DAB-EpCAM were first deparaffinized and rehydrated. Samples were then washed for 5 minutes in water. During this time, citrate antigen retrival buffer was preheated in a microwave for 3 minutes on high power. Samples were then microwaved in the citrate buffer for 10 minutes on high power. Samples were washed with PBS and then blocked for peroxidase activity using Bloxall (*SP6000 VectorLabs*) for 15 minutes at room temperature. Samples were washed three times in PBS. 3 drops of Avidin Block (*004303 Invitrogen*) were added to each slide for 15 minutes at room temperature. Samples were then washed three times with PBS. 3 drops of Biotin Block (*004303 Invitrogen*) were added to each slide for 15 minutes at room temperature.

Samples were rinsed three times in PBS. 3 drops of protein block (*DPB-125 Spring Bioscience*) were added for 30 minutes at room temperature. 120 µl of goat-anti-EpCam (*AbCam ab71916* 1:200) diluted in antibody diluent were added to slides and incubated overnight at 4C. Slides were then washed three times with PBS. 120 µL of biotinylated anti-rabbit secondary antibody diluted 1:500 in antibody diluent and incubated for 30 minutes at room temperature. Sample was then rinsed three times in PBS. 3 drops of Vector RTU ABC reagent were added and incubated for 30 min at room temperature. Samples were then rinsed three times in PBS. 1 drop of DAB was added 1 ml substrate buffer. 120 µL of the DAB working solution were added to each sample and incubated for 4-5 minutes. Samples were washed three times with PBS and then counterstained with haematoxylin for 1 minute. Samples were rinsed with tap water until cleared. Samples were submerged in Scotts water for 20 seconds to blue haematoxylin and rinsed again in tap water. Samples were finally dehydrated to xylene and mounted.

Immunofluorescence

Liver tissue was snap frozen immediately after perfusion using a CoolRack M96-ID freezing block on dry ice. Tissue was sectioned at 8 µm using a cryostat and maintained at -80C until needed. Slides were removed from -80C and immediately fixed for 15 minutes using 10% neutral buffered formalin. Sections were permeabilized for 20 minutes using 0.2% Triton-X 100 PBS (PBST). Sections were then blocked with 2% BSA PBST for 30 minutes. Endogenous biotin was blocked for 15 minutes using streptavidin block (abcam 3387), washed 3 times with PBS, and followed by a 15-minute block with biotin (abcam 3387) to bind any remaining open binding sites on the streptavidin. Sections were washed 3 times with PBST for 5 minutes each. Primary antibodies were diluted in PBST 2% BSA and incubated with sections for 2 hours at RT. Sections were rinsed three times with PBST for five minutes each. Secondary antibodies were diluted in PBST 2% BSA and incubated with sections for 1 hour at RT. Sections were rinsed once with PBST for five minutes. Sections were then stained with 300nM DAPI in PBST for 3 minutes. Sections were rinsed three times with PBST for five minutes each and then mounted for imaging using Fluoromount G (Southern Biotech). Primary antibodies (EpCAM – eBioscience 14-5791-85, 1:100; Ki67- Abcam ab15580, 1:200). Secondary antibodies (Goat anti-Rabbit TRITC – Novex A24536, 1:1000; Goat anti-Rat Alexa Fluor 488 – Invitrogen A11006, 1:1000).

499

500 *Hydroxyproline Quantitation*

501 200-300 mg of tissue was hydrolyzed in 2 mL of 6 N HCl at 110°C for 18 hours. 10 µL
502 of hydrolyzed sample or standard was placed in 30 µL of citric acetate buffer consisting of 10 g
503 citric acid (5% w/v), 2.4 ml Glacial Acetic Acid (1.2% v/v), 14.48 g sodium acetate (7.24% w/v),
504 6.8 g sodium hydroxide (3.4% w/v), made up to 200 ml with sterile, deionized water. 100 µL of
505 Chloramine T solution, consisting of 0.282 g Chloramine T, 2 ml isopropanol, 2 ml sterile water,
506 16 ml citrate acetate buffer, was mixed with the samples or standards and allowed to oxidize for
507 20 minutes at room temperature. 100 µL of Ehrlich's Reagent consisting of 2.5 g of p-
508 dimethylaminobenzaldehyde, 9.3 ml isopropanol, and 3.9 ml 70%-perchloric acid, was mixed
509 with the oxidized samples and standards and allowed to incubate at 65C for 20 minutes.
510 Absorbance was read at 550 nm and compared to the standard curve for quantitation.

511

512 *DNA Isolation and PCR Genotyping*

513 Ear punches from mice or isolated HSCs were suspended in 25 mM NaOH, incubated at
514 95°C for 15 minutes, and then neutralized with 40 mM Tris-HCl. DNA was amplified for 34
515 cycles using GoTaq DNA Polymerase (Promega) according to the manufacturer's instructions.
516 Primers are listed in Supplementary Table 1. Gels were imaged using a BioSpectrum gel viewer
517 with VisionWorksLS software (UVP; Upland, CA). HSCs were isolated as has been described
518 previously (Mederacke et al., 2015).

519

520 *RNA isolation and quantitative RT-PCR*

521 100-200 mg tissue was homogenized in 1mL TRIzol Reagent (Life Technologies; Grand
522 Island, NY) using Precellys 24 (Bertin Technologies; Montigny-le-Bretonneux, France). Total
523 RNA was extracted from the homogenate by addition of 200µL chloroform, vigorous shaking for
524 5 minutes, followed by centrifugation for 20 minutes at 12,000 RPM at 4C. RNA from the
525 aqueous phase was removed and purified using a MagMax-96 Total RNA Isolation Kit (Life
526 Technologies). RNA was reverse transcribed using SuperScript II Reverse Transcriptase (Life
527 Technologies). Real-time RT-PCR was performed on an ABI Prism 7900HT Sequence Detection

System (Applied Biosystems) using the following cycle profile: 95C for 10 minutes followed by 40 cycles of 95C for 15 seconds, 60C for 1 minute. mRNA expression was determined using Power SYBR Green PCR Master Mix (Applied Biosystems), normalized to either 18S mRNA levels. Primers are listed in Supplementary Table 1.

Isolation of Murine Non-parenchymal Cell Fraction and Purification of HPCs

HPCs were isolated and cultured as has been described previously (Lu et al., 2015).

Histological Quantification

Quantification of EpCAM positivity and Ki-67 co-expression was conducted in ImageJ. An intensity filter was used to determine the percent positivity of at least 3, 20x views for each sample. Eosinophils stained with the Wright-Giemsa method and bile duct numbers were scored by a blinded pathologist. Blinding was achieved by covering group labels, randomizing slides, and replacing with labels with numbers. For *S. mansoni* infections, at least 5 granulomas were scored for each sample. For plasmid overexpression experiments, at least 5, 20x views were scored for each sample. ORO pixel percentage was quantified using Leica Aperio Scanscope Software.

Statistical Analyses

Prism 6 was used to compute statistical analyses. Two-tailed Welch's t-tests were used to determine statistical significance between the majority of samples. Samples with very large deviation between means (due to overexpression vectors) used Mann-Whitney U-tests to determine significance. Survival was compared using log-rank (Mantel-Cox) tests. Initial group sizes were estimated based on previous study variance and expected mortality. No statistical methods were used to predetermine sample size. Randomization during processing was achieved by processing mice according to cage (Cre- and Cre+ littermates were not separated). Mice were excluded from 13-OP studies if IL-13 overexpression was not detected by qPCR at time of euthanasia.

Microarrays

RNA isolated as described above was submitted to the NIAID Research Technologies Branch who performed microarray analyses using MouseWG-6 v2.0 and MouseRef-8 v2.0 arrays. Subsequent analyses were performed using TM4 MeV microarray software suite. Welch's t-tests were used to generate volcano plots ($p < 0.05$) from which list subsets were generated by using fold-difference cutoffs. Microarray data have been uploaded to the Gene Expression Omnibus (http://www.ncbi.nlm.nih.gov/geo/) with the accession numbers GSE70704 and GSE70705. Fold change values were uploaded to Ingenuity Pathway Analysis (Qiagen) to determine potential upstream regulators.

Resin Casting

Resin casting was completed as described previously (Walter et al., 2012).

Author Contributions:

Experiments were conceived and designed by RG, TR, LV, and TW. Experiments were performed by RG, TR, KH, KV, DC, and TW. WL and SG conducted DAB-EpCAM staining and provided training for the isolation and culture of HPCs in SFs lab. SF provided $K19^{CreERT/CreERT}Rosa26^{tdTomato/tdTomato}$ mice and pathological expertise. RG performed IPA and statistical analyses. RG, TR, and TW wrote the manuscript.

Acknowledgments:

This research was supported by the Intramural Research Program of the National Institutes of Health, National Institute of Allergy and Infectious Disease. LV is funded by the ERC starting grant Relieve IMDs and the Cambridge Hospitals National Institute for Health Research Biomedical Research Center. The funders had no role in study design, data collection and analysis, decision to publish, or preparation of the manuscript. The authors declare no competing financial interests. We thank Frank Brombacher for sharing the IL4Rα-floxed mice.

584

585 **References:**

586 Alison, M.R., and Lovell, M.J. (2005). Liver cancer: the role of stem cells. Cell Prolif *38*, 407-
587 421.
588 Beck, L.A., Thaci, D., Hamilton, J.D., Graham, N.M., Bieber, T., Rocklin, R., Ming, J.E., Ren,
589 H., Kao, R., Simpson, E.*, et al.* (2014). Dupilumab treatment in adults with moderate-to-severe
590 atopic dermatitis. The New England journal of medicine *371*, 130-139.
591 Borthwick, L.A., Barron, L., Hart, K.M., Vannella, K.M., Thompson, R.W., Oland, S., Cheever,
592 A., Sciurba, J., Ramalingam, T.R., Fisher, A.J., and Wynn, T.A. (2015). Macrophages are critical
593 to the maintenance of IL-13-dependent lung inflammation and fibrosis. Mucosal immunology.
594 Brightling, C.E., Chanez, P., Leigh, R., O'Byrne, P.M., Korn, S., She, D., May, R.D., Streicher,
595 K., Ranade, K., and Piper, E. (2015). Efficacy and safety of tralokinumab in patients with severe
596 uncontrolled asthma: a randomised, double-blind, placebo-controlled, phase 2b trial. The Lancet.
597 Respiratory medicine *3*, 692-701.
598 Chandriani, S., DePianto, D.J., N'Diaye, E.N., Abbas, A.R., Jackman, J., Bevers, J., Ramirez-
599 Carrozzi, V., Pappu, R., Kauder, S.E., Toy, K.*, et al.* (2014). Endogenously Expressed IL-13R
600 alpha 2 Attenuates IL-13-Mediated Responses but Does Not Activate Signaling in Human Lung
601 Fibroblasts. J Immunol *193*, 111-119.
602 Chen, F., Liu, Z., Wu, W., Rozo, C., Bowdridge, S., Millman, A., Van Rooijen, N., Urban, J.F.,
603 Jr., Wynn, T.A., and Gause, W.C. (2012). An essential role for TH2-type responses in limiting
604 acute tissue damage during experimental helminth infection. Nat Med *18*, 260-266.
605 Chiaramonte, M.G., Donaldson, D.D., Cheever, A.W., and Wynn, T.A. (1999). An IL-13
606 inhibitor blocks the development of hepatic fibrosis during a T-helper type 2-dominated
607 inflammatory response. Journal of Clinical Investigation *104*, 777-785.
608 Chiaramonte, M.G., Mentink-Kane, M., Jacobson, B.A., Cheever, A.W., Whitters, M.J., Goad,
609 M.E.P., Wong, A., Collins, M., Donaldson, D.D., Grusby, M.J., and Wynn, T.A. (2003).
610 Regulation and function of the interleukin 13 receptor alpha 2 during a T helper cell type 2-
611 dominant immune response. J Exp Med *197*, 687-701.
612 Choy, D.F., Hart, K.M., Borthwick, L.A., Shikotra, A., Nagarkar, D.R., Siddiqui, S., Jia, G.Q.,
613 Ohri, C.M., Doran, E., Vannella, K.M.*, et al.* (2015). T(H)2 and T(H)17 inflammatory pathways
614 are reciprocally regulated in asthma. Sci Transl Med *7*.
615 Clouston, A.D., Powell, E.E., Walsh, M.J., Richardson, M.M., Demetris, A.J., and Jonsson, J.R.
616 (2005). Fibrosis correlates with a ductular reaction in hepatitis C: roles of impaired replication,
617 progenitor cells and steatosis. Hepatology (Baltimore, Md) *41*, 809-818.
618 Danese, S., Rudzinski, J., Brandt, W., Dupas, J.L., Peyrin-Biroulet, L., Bouhnik, Y.,
619 Kleczkowski, D., Uebel, P., Lukas, M., Knutsson, M.*, et al.* (2015). Tralokinumab for moderate-
620 to-severe UC: a randomised, double-blind, placebo-controlled, phase IIa study. Gut *64*, 243-249.
621 Farber, E. (1956). Similarities in the sequence of early histological changes induced in the liver
622 of the rat by ethionine, 2-acetylamino-fluorene, and 3'-methyl-4-dimethylaminoazobenzene.
623 Cancer Res *16*, 142-148.
624 Font-Burgada, J., Shalapour, S., Ramaswamy, S., Hsueh, B., Rossell, D., Umemura, A.,
625 Taniguchi, K., Nakagawa, H., Valasek, M.A., Ye, L.*, et al.* (2015). Hybrid Periportal
626 Hepatocytes Regenerate the Injured Liver without Giving Rise to Cancer. Cell *162*, 766-779.

627 Foo, S.S., Turner, C.J., Adams, S., Compagni, A., Aubyn, D., Kogata, N., Lindblom, P., Shani,
628 M., Zicha, D., and Adams, R.H. (2006). Ephrin-B2 controls cell motility and adhesion during
629 blood-vessel-wall assembly. Cell *124*, 161-173.
630 Fukushi, J., Ono, M., Morikawa, W., Iwamoto, Y., and Kuwano, W. (2000). The activity of
631 soluble VCAM-1 in angiogenesis stimulated by IL-4 and IL-13. J Immunol *165*, 2818-2823.
632 Goh, Y.P.S., Henderson, N.C., Heredia, J.E., Eagle, A.R., Odegaard, J.I., Lehwald, N., Nguyen,
633 K.D., Sheppard, D., Mukundan, L., Locksley, R.M., and Chawla, A. (2013). Eosinophils secrete
634 IL-4 to facilitate liver regeneration. P Natl Acad Sci USA *110*, 9914-9919.
635 Hamilton, J.D., Suarez-Farinas, M., Dhingra, N., Cardinale, I., Li, X., Kostic, A., Ming, J.E.,
636 Radin, A.R., Krueger, J.G., Graham, N.*, et al.* (2014). Dupilumab improves the molecular
637 signature in skin of patients with moderate-to-severe atopic dermatitis. The Journal of allergy
638 and clinical immunology *134*, 1293-1300.
639 Heller, F., Florian, P., Bojarski, C., Richter, J., Christ, M., Hillenbrand, B., Mankertz, J., Gitter,
640 A.H., Burgel, N., Fromm, M.*, et al.* (2005). Interleukin-13 is the key effector Th2 cytokine in
641 ulcerative colitis that affects epithelial tight junctions, apoptosis, and cell restitution.
642 Gastroenterology *129*, 550-564.
643 Henderson, N.C., Arnold, T.D., Katamura, Y., Giacomini, M.M., Rodriguez, J.D., McCarty, J.H.,
644 Pellicoro, A., Raschperger, E., Betsholtz, C., Ruminski, P.G.*, et al.* (2013). Targeting of alpha(v)
645 integrin identifies a core molecular pathway that regulates fibrosis in several organs. Nat Med
646 *19*, 1617-1624.
647 Huch, M., Gehart, H., van Boxtel, R., Hamer, K., Blokzijl, F., Verstegen, M.M., Ellis, E., van
648 Wenum, M., Fuchs, S.A., de Ligt, J.*, et al.* (2015). Long-term culture of genome-stable bipotent
649 stem cells from adult human liver. Cell *160*, 299-312.
650 Jors, S., Jeliazkova, P., Ringelhan, M., Thalhammer, J., Durl, S., Ferrer, J., Sander, M.,
651 Heikenwalder, M., Schmid, R.M., Siveke, J.T., and Geisler, F. (2015). Lineage fate of ductular
652 reactions in liver injury and carcinogenesis. The Journal of clinical investigation.
653 Karimian, N., op den Dries, S., and Porte, R.J. (2013). The origin of biliary strictures after liver
654 transplantation: Is it the amount of epithelial injury or insufficient regeneration that counts?
655 Journal of hepatology *58*, 1065-1067.
656 Kaviratne, M., Hesse, M., Leusink, M., Cheever, A.W., Davies, S.J., McKerrow, J.H.,
657 Wakefield, L.M., Letterio, J.J., and Wynn, T.A. (2004). IL-13 activates a mechanism of tissue
658 fibrosis that is completely TGF-beta independent. Journal of immunology *173*, 4020-4029.
659 Landi, A., Weismuller, T.J., Lankisch, T.O., Santer, D.M., Tyrrell, D.L.J., Manns, M.P., and
660 Houghton, M. (2014). Differential Serum Levels of Eosinophilic Eotaxins in Primary Sclerosing
661 Cholangitis, Primary Biliary Cirrhosis, and Autoimmune Hepatitis. J Interf Cytok Res *34*, 204-
662 214.
663 Li, J., Bessho, K., Shivakumar, P., Mourya, R., Mohanty, S.K., dos Santos, J.L., Miura, I.K.,
664 Porta, G., and Bezerra, J.A. (2011). Th2 signals induce epithelial injury in mice and are
665 compatible with the biliary atresia phenotype. Journal of Clinical Investigation *121*, 4244-4256.
666 Li, J., Razumilava, N., Gores, G.J., Walters, S., Mizuochi, T., Mourya, R., Bessho, K., Wang,
667 Y.H., Glaser, S.S., Shivakumar, P., and Bezerra, J.A. (2014). Biliary repair and carcinogenesis
668 are mediated by IL-33-dependent cholangiocyte proliferation. The Journal of clinical
669 investigation *124*, 3241-3251.
670 Lin, J., Lu, F.K., Zheng, W., Xu, S.Y., Tai, D.A., Yu, H., and Huang, Z.W. (2011). Assessment
671 of liver steatosis and fibrosis in rats using integrated coherent anti-Stokes Raman scattering and
672 multiphoton imaging technique. J Biomed Opt *16*.

673 Liu, F., Song, Y.K., and Liu, D. (1999). Hydrodynamics-based transfection in animals by
674 systemic administration of plasmid DNA. Gene Ther *6*, 1258-1266.
675 Liu, Y., Meyer, C., Muller, A., Herweck, F., Li, Q., Mullenbach, R., Mertens, P.R., Dooley, S.,
676 and Weng, H.L. (2011). IL-13 Induces Connective Tissue Growth Factor in Rat Hepatic Stellate
677 Cells via TGF-beta-Independent Smad Signaling. J Immunol *187*, 2814-2823.
678 Lowes, K.N., Brennan, B.A., Yeoh, G.C., and Olynyk, J.K. (1999). Oval cell numbers in human
679 chronic liver diseases are directly related to disease severity. Am J Pathol *154*, 537-541.
680 Lu, W.Y., Bird, T.G., Boulter, L., Tsuchiya, A., Cole, A.M., Hay, T., Guest, R.V., Wojtacha, D.,
681 Man, T.Y., Mackinnon, A.*, et al.* (2015). Hepatic progenitor cells of biliary origin with liver
682 repopulation capacity. Nat Cell Biol *17*, 971-983.
683 Means, A.L., Xu, Y., Zhao, A., Ray, K.C., and Gu, G. (2008). A CK19(CreERT) knockin mouse
684 line allows for conditional DNA recombination in epithelial cells in multiple endodermal organs.
685 Genesis *46*, 318-323.
686 Mederacke, I., Dapito, D.H., Affo, S., Uchinami, H., and Schwabe, R.F. (2015). High-yield and
687 high-purity isolation of hepatic stellate cells from normal and fibrotic mouse livers. Nat Protoc
688 *10*, 305-315.
689 Metwally, S.S., Mosaad, Y.M., Abdel-Samee, E.R., El-Gayyar, M.A., Abdel-Aziz, A.M., and El-
690 Chennawi, F.A. (2004). IL-13 gene expression in patients with atopic dermatitis: relation to IgE
691 level and to disease severity. The Egyptian journal of immunology / Egyptian Association of
692 Immunologists *11*, 171-177.
693 Murray, L.A., Zhang, H.L., Oak, S.R., Coelho, A.L., Herath, A., Flaherty, K.R., Lee, J., Bell, M.,
694 Knight, D.A., Martinez, F.J.*, et al.* (2014). Targeting Interleukin-13 with Tralokinumab
695 Attenuates Lung Fibrosis and Epithelial Damage in a Humanized SCID Idiopathic Pulmonary
696 Fibrosis Model. Am J Resp Cell Mol *50*, 985-994.
697 Park, Y.N., Kojiro, M., Di Tommaso, L., Dhillon, A.P., Kondo, F., Nakano, M., Sakamoto, M.,
698 Theise, N.D., and Roncalli, M. (2007). Ductular reaction is helpful in defining early stromal
699 invasion, small hepatocellular carcinomas, and dysplastic nodules. Cancer *109*, 915-923.
700 Pearce, E.J., and MacDonald, A.S. (2002). The immunobiology of schistosomiasis. Nat Rev
701 Immunol *2*, 499-511.
702 Ramalingam, T.R., Pesce, J.T., Sheikh, F., Cheever, A.W., Mentink-Kane, M.M., Wilson, M.S.,
703 Stevens, S., Valenzuela, D.M., Murphy, A.J., Yancopoulos, G.D.*, et al.* (2008). Unique functions
704 of the type II interleukin 4 receptor identified in mice lacking the interleukin 13 receptor alpha1
705 chain. Nat Immunol *9*, 25-33.
706 Reiman, R.M., Thompson, R.W., Feng, C.G., Hari, D., Knight, R., Cheever, A.W., Rosenberg,
707 H.F., and Wynn, T.A. (2006). Interleukin-5 (IL-5) augments the progression of liver fibrosis by
708 regulating IL-13 activity. Infect Immun *74*, 1471-1479.
709 Ricardo-Gonzalez, R.R., Red Eagle, A., Odegaard, J.I., Jouihan, H., Morel, C.R., Heredia, J.E.,
710 Mukundan, L., Wu, D., Locksley, R.M., and Chawla, A. (2010). IL-4/STAT6 immune axis
711 regulates peripheral nutrient metabolism and insulin sensitivity. Proc Natl Acad Sci U S A *107*,
712 22617-22622.
713 Richardson, M.M., Jonsson, J.R., Powell, E.E., Brunt, E.M., Neuschwander-Tetri, B.A., Bhathal,
714 P.S., Dixon, J.B., Weltman, M.D., Tilg, H., Moschen, A.R.*, et al.* (2007). Progressive fibrosis in
715 nonalcoholic steatohepatitis: association with altered regeneration and a ductular reaction.
716 Gastroenterology *133*, 80-90.
717 Roskams, T. (2006). Liver stem cells and their implication in hepatocellular and
718 cholangiocarcinoma. Oncogene *25*, 3818-3822.

719 Roskams, T.A., Theise, N.D., Balabaud, C., Bhagat, G., Bhathal, P.S., Bioulac-Sage, P., Brunt,
720 E.M., Crawford, J.M., Crosby, H.A., Desmet, V.*, et al.* (2004). Nomenclature of the finer
721 branches of the biliary tree: canals, ductules, and ductular reactions in human livers. Hepatology
722 (Baltimore, Md) *39*, 1739-1745.
723 Sancho-Bru, P., Altamirano, J., Rodrigo-Torres, D., Coll, M., Millan, C., Lozano, J.J., Miquel,
724 R., Arroyo, V., Caballeria, J., Gines, P., and Bataller, R. (2012). Liver progenitor cell markers
725 correlate with liver damage and predict short-term mortality in patients with alcoholic hepatitis.
726 Hepatology *55*, 1931-1941.
727 Schaap, F.G., van der Gaag, N.A., Gouma, D.J., and Jansen, P.L. (2009). High expression of the
728 bile salt-homeostatic hormone fibroblast growth factor 19 in the liver of patients with
729 extrahepatic cholestasis. Hepatology *49*, 1228-1235.
730 Scheerens, H., Arron, J.R., Zheng, Y., Putnam, W.S., Erickson, R.W., Choy, D.F., Harris, J.M.,
731 Lee, J., Jarjour, N.N., and Matthews, J.G. (2014). The effects of lebrikizumab in patients with
732 mild asthma following whole lung allergen challenge. Clin Exp Allergy *44*, 38-46.
733 Shimamura, T., Fujisawa, T., Husain, S.R., Kioi, M., Nakajima, A., and Puri, R.K. (2008). Novel
734 role of IL-13 in fibrosis induced by nonalcoholic steatohepatitis and its amelioration by IL-13R-
735 directed cytotoxin in a rat model. J Immunol *181*, 4656-4665.
736 Sorrentino, P., Terracciano, L., D'Angelo, S., Ferbo, U., Bracigliano, A., Tarantino, L., Perrella,
737 A., Perrella, O., De Chiara, G., Panico, L.*, et al.* (2010). Oxidative stress and steatosis are
738 cofactors of liver injury in primary biliary cirrhosis. Journal of gastroenterology *45*, 1053-1062.
739 Sparks, E.E., Huppert, K.A., Brown, M.A., Washington, M.K., and Huppert, S.S. (2010). Notch
740 Signaling Regulates Formation of the Three-Dimensional Architecture of Intrahepatic Bile Ducts
741 in Mice. Hepatology *51*, 1391-1400.
742 Stanya, K.J., Jacobi, D., Liu, S., Bhargava, P., Dai, L., Gangl, M.R., Inouye, K., Barlow, J.L., Ji,
743 Y., Mizgerd, J.P.*, et al.* (2013). Direct control of hepatic glucose production by interleukin-13 in
744 mice. J Clin Invest *123*, 261-271.
745 Sugimoto, R., Enjoji, M., Nakamuta, M., Ohta, S., Kohjima, M., Fukushima, M., Kuniyoshi, M.,
746 Arimura, E., Morizono, S., Kotoh, K., and Nawata, H. (2005). Effect of IL-4 and IL-13 on
747 collagen production in cultured LI90 human hepatic stellate cells. Liver Int *25*, 420-428.
748 Walter, T.J., Sparks, E.E., and Huppert, S.S. (2012). 3-dimensional resin casting and imaging of
749 mouse portal vein or intrahepatic bile duct system. Journal of visualized experiments : JoVE,
750 e4272.
751 Wang, B., Zhao, L.D., Fish, M., Logan, C.Y., and Nusse, R. (2015). Self-renewing diploid
752 Axin2(+) cells fuel homeostatic renewal of the liver. Nature *524*, 180-+.
753 Wenzel, S., Ford, L., Pearlman, D., Spector, S., Sher, L., Skobieranda, F., Wang, L., Kirkesseli,
754 S., Rocklin, R., Bock, B.*, et al.* (2013). Dupilumab in persistent asthma with elevated eosinophil
755 levels. The New England journal of medicine *368*, 2455-2466.
756 Wynn, T.A. (2015). Type 2 cytokines: mechanisms and therapeutic strategies. Nat Rev Immunol
757 *15*, 271-282.
758 Yanger, K., Knigin, D., Zong, Y., Maggs, L., Gu, G., Akiyama, H., Pikarsky, E., and Stanger,
759 B.Z. (2014). Adult hepatocytes are generated by self-duplication rather than stem cell
760 differentiation. Cell Stem Cell *15*, 340-349.
761 Yoon, S.M., Gerasimidou, D., Kuwahara, R., Hytiroglou, P., Yoo, J.E., Park, Y.N., and Theise,
762 N.D. (2011). Epithelial Cell Adhesion Molecule (EpCAM) Marks Hepatocytes Newly Derived
763 from Stem/Progenitor Cells in Humans. Hepatology *53*, 964-973.

Figure Legends:

Figure 1. IL-4/13 Signaling in Hepatocytes and/or Biliary Cells Drive DR.
(**A**) Assessment of collagen deposition by hydroxyproline quantitation of naïve mice and mice infected with *S. mansoni* for 10 or 18 weeks. N-values left to right: n = 5, 5, 8, 7, 12, 11.
(**B**) Picrosirius red stain visualizing quality of fibrotic deposition in mice infected for 18 weeks.
(**C**) DAB-EpCAM immunohistochemistry of mice infected for 10 and 18 weeks highlighting peri-granuloma DR.
(**D**) Quantitation of $EpCAM^+$ pixels per randomly chosen 20X microscopic field view. N-values left to right: n = 9, 9, 11, 15, 10, 14.
(**E**) Quantitation of liver weights of naïve mice and mice infected for 10 or 18 weeks. N-values left to right: n = 5, 5, 8, 7, 12, 11.
(**F**) Quantitation of ductular reaction as assessed by percentage of $EpCAM^+$ cells per randomly chosen 20X microscopic field view co-expressing Ki-67 at 18 weeks. N-values left to right: n = 9, 9.
(**G**) Quantification of serum alanine transaminase (ALT) and aspartate transaminase (AST). Serum was taken from ongoing infections at 4, 8, and 12 weeks. Serum from the 18-week time point was obtained at the time of euthanasia. N-values left to right: n = 40, 41, 24, 29, 16, 11, 9, 7.
(**H**) Ki-67/EpCAM immunostaining with DAPI nuclear counterstain of mice infected for 18 weeks.
(**I**) Oil Red O staining highlighting microvesicular lipid droplets after 18 weeks.
(**J**) Alb-Cre^- animals exhibit DR, steatosis, and fibrosis after infection with *S. mansoni.* In contrast, Alb-Cre^+ animals, in which IL-4/13 signaling is blocked in hepatocytes and cholangiocytes, do not develop significant DR or steatosis yet still have significant fibrosis.
(Note) Results representative of three replicate experiments; All scale bars 100 μm; SME: non-specific staining due of *S. mansoni* eggs; DR: Ductular Reaction; results reported as mean ± S.E.M.; $p^*<0.05$, $p^{**}<0.01$, $p^{***}<0.001$, $p^{****}<0.0001$.

Figure 2. IL-13 is Necessary for DR during S. Mansoni Infection.

(**A, B**) Wright-Giemsa staining of 18-week infected (**A**) Alb-Cre^{-} and (**B**) Alb-Cre^{-} mice highlighting bile ducts.

(**C-E**) Wright-Giemsa staining of 12-week infected (**C**) IL13Rα1$^{-/-}$, (**D**) IL-13$^{-/-}$, (**E**) IL-4$^{-/-}$ mice highlighting bile ducts.

(**F**) Quantitation of number of bile ducts pixels per randomly chosen 20X microscopic field view. N-values left to right: n = 35, 40, 70, 40, 15, 75. Data is presented as mean ± SEM of at least 5 fields per mouse from at least 3 mice per group.

(**G**) Schematic illustrating the signaling pathways blocked and active in each of the knockout models. IL13Rα1$^{-/-}$ mice, in which all IL-13 signaling is blocked and IL-4 can only signal through the type-1 receptor complex, fail to develop DR, demonstrating that the type-1 receptor is not involved in DR. Similarly, IL-13$^{-/-}$ mice, in which IL-4 signaling is normal, fail to develop DR, demonstrating that IL-4 is not involved in DR. However, IL-4$^{-/-}$ mice, in which IL-13 signaling is normal, develop florid DRs, suggesting a crucial role for IL-13 in the pathogenesis of DR.

(Note) All scale bars 100 μm; Arrows highlight bile ducts; p*<0.05, p**<0.01, p***<0.001, p****<0.0001.

Figure 3. IL-13 Signaling in Hepatocytes and/or Biliary Cells Induces DR.

(**A**) Quantitation of mRNA expression by qPCR of IL-13 responsive genes relative to *18S* of mice injected with an eGFP or IL-13 overexpression plasmid after 9 days. N-values left to right: n = 5, 5, 8, 6.

(**B**) Assessment of collagen deposition by hydroxyproline quantitation. N-values left to right: n = 5, 5, 8, 6.

(**C**) Picrosirius red staining visualizing fibrotic deposition.

(**D**) Quantitation of ductular reaction as percentage of EpCAM^{+} cells per randomly chosen 20X microscopic field view co-expressing Ki-67. N-values left to right: n = 9, 9.

(**E**) Quantitation of percentage of ORO strong positive pixels per randomly selected 20X view. N-values left to right: n = 9, 9.

(**F**) Quantification of serum triglycerides taken at the time of euthanasia. N-values left to right: n = 8, 6.

(**G**) Ki-67/EpCAM immunostaining with DAPI nuclear counterstain of IL-13 overexpression mice.
(**H**) Oil Red O staining highlighting steatotic lipid droplets of IL-13 overexpression mice.
(**I**) Subset of Illumina Beadchip microarray analysis showing genes selected using the following criteria: $p < 0.01$ (Welch's t-test, Alb-Cre$^+$ IL-13 v. Alb-Cre$^-$ IL-13), |Fold Difference| > 2 (Alb-Cre$^+$ IL-13 v. Alb-Cre$^-$ IL-13).
(**J**) Select pathways significantly perturbed by IL-13 signaling through Alb$^+$ cells ($p < 0.01$).
(**K**) Ingenuity Pathway Analysis was utilized to identify differences in key downstream downstream mediators of metabolism, senescence, and bile acid synthesis in the Alb-Cre$^-$ mice compared to the Alb-Cre$^+$ mice.
(**L**) Quantitation of mRNA expression by qPCR of select metabolism, bile synthesis/excretion, and inflammation-related genes identified by microarray analysis. N-values left to right: n = 5, 5, 8, 6.
(Note) Data representative of two replicate experiments reported as mean ± S.E.M.; All scale bars 100 μm; Arrows point to bile ducts; p*<0.05, p**<0.01, p***<0.001, p****<0.0001.

Figure 4. Direct IL-13 Signaling in K19$^+$ Cells Induces DR and Steatosis.
(**A**) Assessment of collagen deposition by hydroxyproline quantitation of mice injected with an eGFP or IL-13 overexpression plasmid after 1 week. N-values left to right: n = 3, 4, 4, 6.
(**B**) Picrosirius red staining visualizing quality of fibrotic deposition.
(**C**) Quantitation of mRNA expression by qPCR of IL-13 responsive genes relative to *18S*. N-values left to right: n = 3, 4, 4, 6.
(**D**) Quantitation of ductular reaction as assessed by percentage of EpCAM$^+$ cells per randomly chosen 20X microscopic field view co-expressing Ki-67. N-values left to right: n = 9, 9.
(**E**) Ki-67/EpCAM immunostaining with DAPI nuclear counterstain of IL-13 overexpression mice.
(**F**) Quantitation of percentage of ORO strong positive pixels per randomly selected 20X view. N-values left to right: n = 9, 9.
(**G**) Oil Red O staining highlighting steatotic lipid droplets of IL-13 overexpression mice after 9 days.

(**H**) K19-Cre$^-$ animals exhibit DR, steatosis, and fibrosis after 13-OP. In contrast, K19-Cre$^+$ animals, in which IL-13 signaling is blocked in cholangiocytes, but not hepatocytes and other cells, do not develop significant DR or steatosis, yet still have significant fibrosis.
(**I**) Assessment of collagen deposition by hydroxyproline quantitation of infected with *S. mansoni* for 12 weeks. N-values left to right: n = 14, 8.
(**J**) Picrosirius red staining visualizing quality of fibrotic deposition.
(**K**) Quantitation of liver weights of mice infected for 12 weeks. N-values left to right: n = 14, 8.
(**L**) Infection Burden as assessed by number of mature worm pairs recovered after perfusion of the liver at time of euthanasia. N-values left to right: n = 14, 8.
(**M**) Quantitation of ductular reaction as assessed by percentage of EpCAM$^+$ cells per randomly chosen 20X microscopic field view co-expressing Ki-67. N-values left to right: n = 8, 10.
(**N**) Ki-67/EpCAM immunostaining with DAPI nuclear counterstain of infected mice.
(**O**) Quantification of serum alanine transaminase (ALT) and aspartate transaminase (AST) obtained at the time of euthanasia. N-values left to right: n = 14, 8.
(Note) Data representative of two replicate experiments; All scale bars 100 μm; Arrows point to bile ducts; p*<0.05, p**<0.01, p***<0.001, p****<0.0001.

Figure 5. IL-13 Signaling through PDGFRB$^+$ Fibroblasts is Necessary for IL-13 Driven Fibrosis.
(**A**) Assessment of collagen deposition by hydroxyproline quantitation of mice injected with an eGFP or IL-13 overexpression plasmid after 1 week. N-values left to right: n = 3, 3, 4, 8.
(**B**) Picrosirius red staining visualizing fibrotic deposition.
(**C**) Quantitation of mRNA expression by qPCR of IL-13 responsive genes relative to *18S*. N-values left to right: n = 3, 3, 4, 8.
(**D**) Oil Red O staining highlighting steatotic lipid droplets of IL-13 overexpression mice after 9 days.
(**E**) Ki-67/EpCAM immunostaining with DAPI nuclear counterstain of IL-13 overexpression mice highlighting ductular proliferation.
(**F**) Assessment of collagen deposition by hydroxyproline quantitation of mice infected with *S. mansoni* for 12 weeks. N-values left to right: n = 6, 4.
(**G**) Picrosirius red staining visualizing fibrotic deposition in mice infected for 12 weeks.

(**H**) Ki-67/EpCAM immunostaining with DAPI nuclear counterstain of mice infected for 12 weeks highlighting ductular proliferation.
(**I**) Schematic illustrating the different cell types targeted by IL-13 and downstream phenomenon related to each cell type.
(Note) *S. mansoni* data representative of two replicate experiments; All scale bars 100 μm; p*<0.05, p**<0.01, p***<0.001, p****<0.0001.

Figure 6. IL-13 Signaling in Hepatocytes and Fibroblasts Assists in the Recruitment of Eosinophils.
(**A**) Wright-Giemsa Staining used to quantify eosinophils (pink staining).
(**B**) Quantitation of number of eosinophils per randomly chosen 20X microscopic field view. Data is presented as mean ± SEM of 5 fields per mouse from at least 3 mice per group.
(**C**) Quantitation of eotaxin-1 (ccl11) mRNA expression by qPCR relative to *18S*. N-values left to right: Alb-Cre: n = 5, 5, 8, 6; K19-Cre: n = 3, 4, 4, 6; PDGFRB-Cre: n = 3, 3, 4, 8.
(**D**) Schematic illustrating the role of fibroblasts and hepatocytes in recruiting eosinophils through the IL-13 induced expression of eotaxin-1.
(Note) All scale bars 100 μm; Arrows point to bile ducts; p*<0.05, p**<0.01, p***<0.001, p****<0.0001.

Figure 7. IL-13 Driven DR Initiates Ductal Cholestasis Independently from Fibrosis.
(**A**) Picrosirius red staining visualizing fibrotic deposition and highlighting the accumulation of yellow cholesterol crystals in Alb-Cre$^-$ mice.
(**B**) Picrosirius red staining visualizing fibrotic deposition and highlighting the accumulation of yellow cholesterol in K19-Cre$^-$ mice.
(**C**) Picrosirius red staining visualizing fibrotic deposition in PDGFRB-Cre$^-$ and highlighting the accumulation of yellow cholesterol crystals in both PDGFRB-Cre$^-$ and PDGFRB-Cre$^+$ mice.
(**D**) EpCAM/Ki-67 co-staining demonstrating that bile ducts in mice overexpressing IL-13 proliferate to the point of occluding bile ducts (arrow).
(**E**) Resin casting of biliary trees from WT and 13-OP mice demonstrate a truncated biliary tree in 13-OP treated mice as a result of proliferation-induced ductal occlusion.

(**F**) Schematic illustrating the role of ductular proliferation in inducing cholestasis through the occlusion of large branching ducts, and subsequent induction of a pro-lipogenic program within hepatocytes resulting in steatosis.

(Note) All scale bars 100 μm.

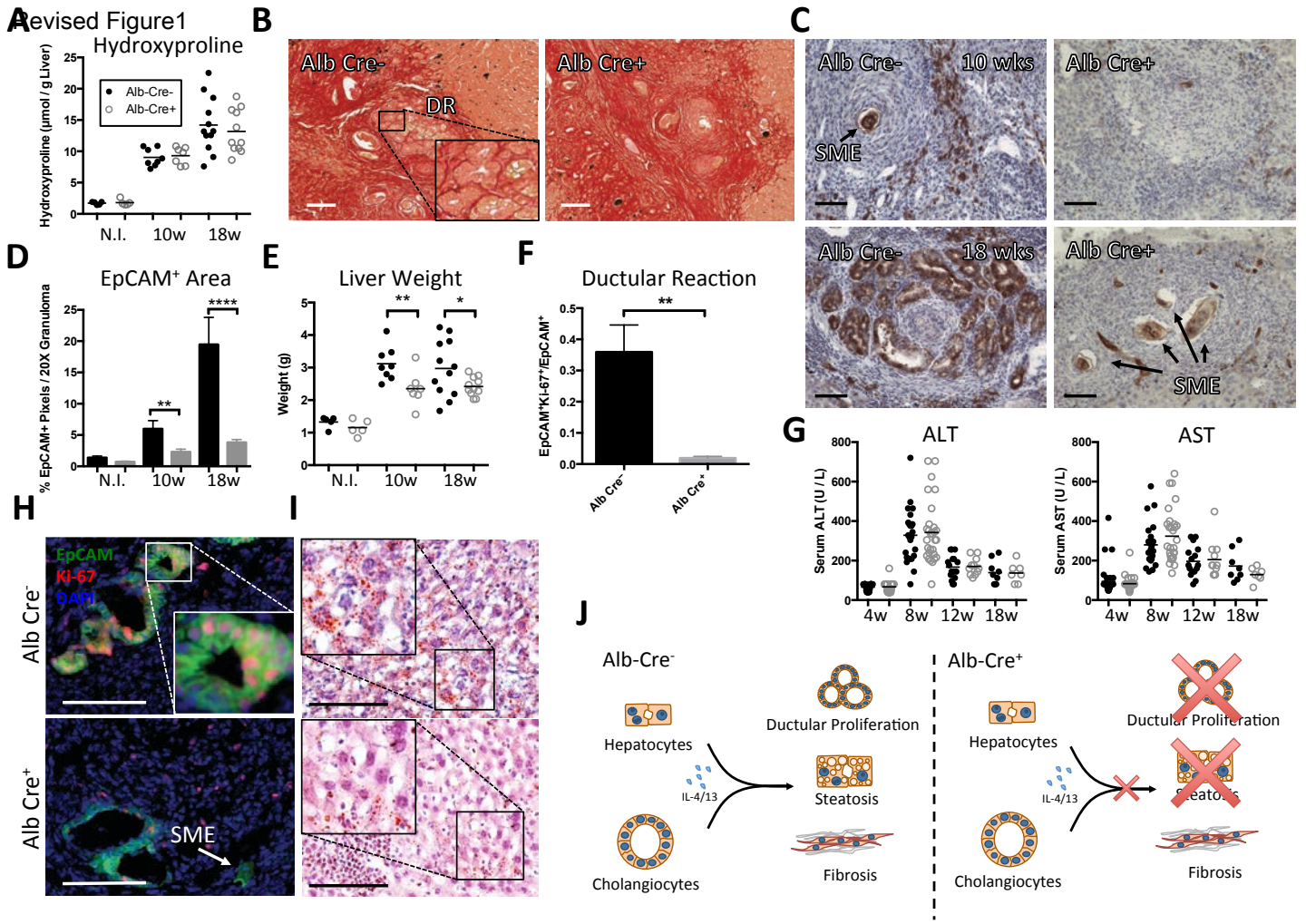
A
Revised Figure1
Hydroxyproline
Hydroxyproline (µmol / g Liver)
Alb-Cre-
Alb-Cre+
N.I.
10w
18w
B
Alb Cre-
Alb Cre+
DR
C
Alb Cre-
10 wks
Alb Cre+
SME
Alb Cre-
18 wks
Alb Cre+
SME
D
EpCAM+ Area
% EpCAM+ Pixels / 20X Granuloma
E
Liver Weight
Weight (g)
F
Ductular Reaction
EpCAM+Ki-67+/EpCAM+
Alb Cre-
Alb Cre+
G
ALT
Serum ALT (U / L)
AST
Serum AST (U / L)
4w
8w
12w
18w
H
EpCAM
Ki-67
DAPI
Alb Cre-
Alb Cre+
SME
I
J
Alb-Cre-
Hepatocytes
Cholangiocytes
IL-4/13
Ductular Proliferation
Steatosis
Fibrosis
Alb-Cre+
Hepatocytes
Cholangiocytes
IL-4/13
Ductular Proliferation
Fibrosis

Figure 1

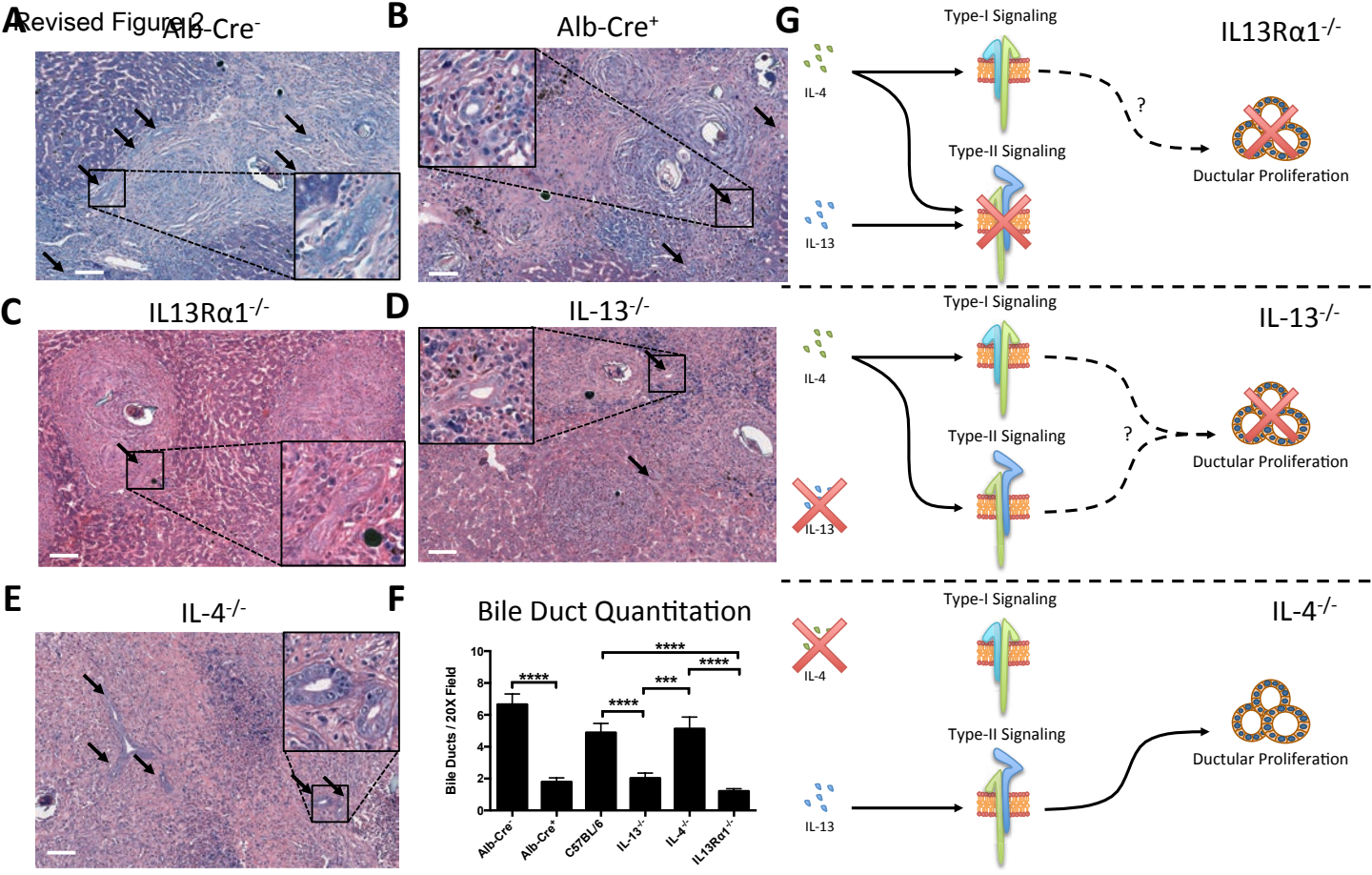
A
Alb-Cre-
B
Alb-Cre+
C
IL13Rα1-/-
D
IL-13-/-
E
IL-4-/-
F
Bile Duct Quantitation
Bile Ducts / 20X Field
10
8
6
4
2
0
****
****
****
***
****
Alb-Cre-
Alb-Cre+
C57BL/6
IL-13-/-
IL-4-/-
IL13Rα1-/-
G
Type-I Signaling
IL-4
Type-II Signaling
IL-13
?
Ductular Proliferation
IL13Rα1-/-
Type-I Signaling
IL-4
Type-II Signaling
IL-13
?
Ductular Proliferation
IL-13-/-
Type-I Signaling
IL-4
Type-II Signaling
IL-13
Ductular Proliferation
IL-4-/-

Figure 2

Revised Figure 3

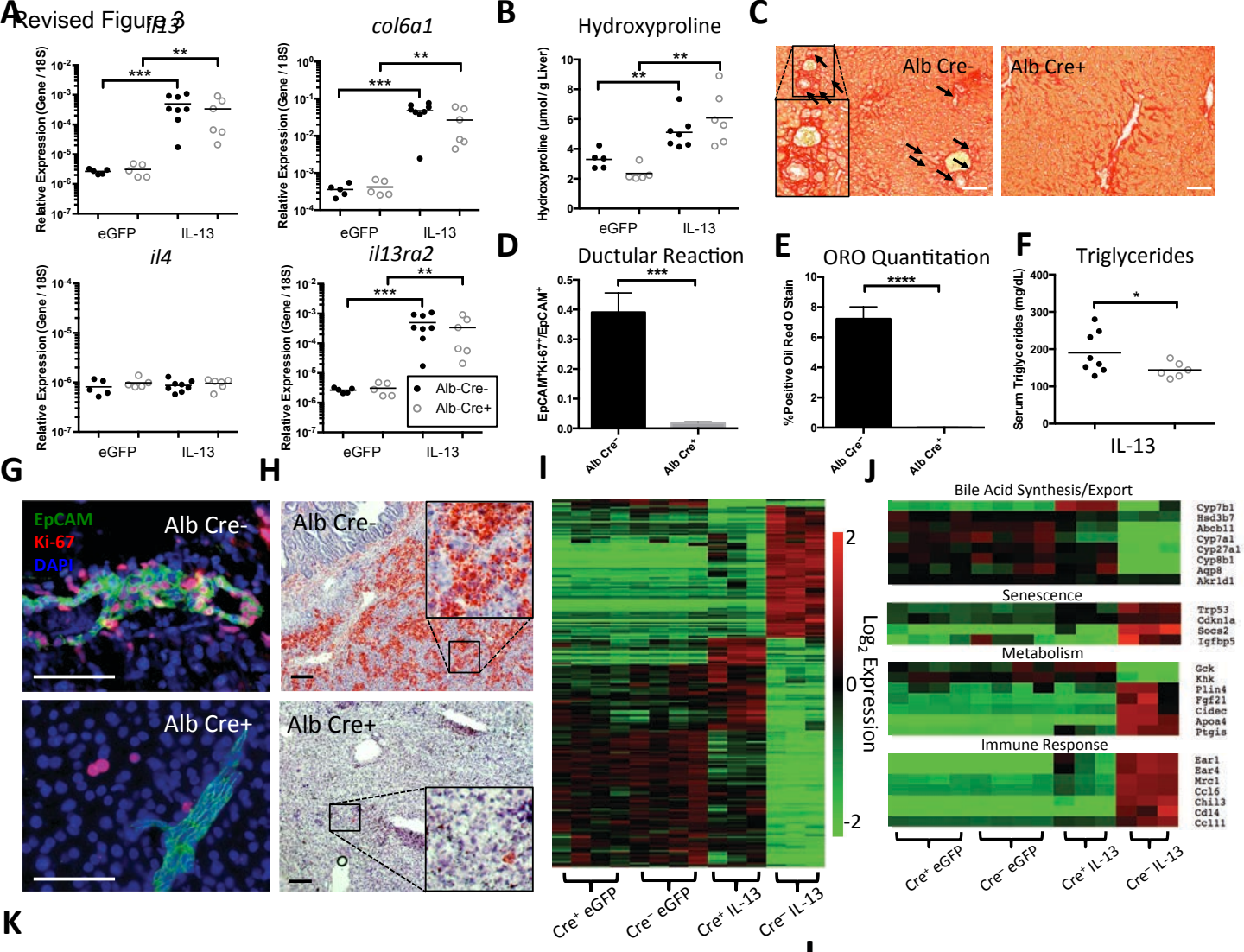

K

Gene	Pred. Activation	p-value	Z-Score
IL1B	ACTIVATED	1.93E-14	4.903
POR	ACTIVATED	4.67E-40	3.897
TNF	ACTIVATED	2.93E-16	3.871
IL6	ACTIVATED	8.06E-10	3.849
PPARA	ACTIVATED	3.28E-44	3.313
IL1A	ACTIVATED	8.29E-07	3.147
IL5	ACTIVATED	3.48E-08	2.912
IL1	ACTIVATED	2.10E-06	2.902
INSIG	ACTIVATED	1.09E-19	2.825
INFG	ACTIVATED	1.26E-08	2.727
STAT3	ACTIVATED	1.49E-06	2.666
CNTF	ACTIVATED	2.15E-06	2.562
IL17A	ACTIVATED	7.31E-06	2.471
CYP51A1	ACTIVATED	1.63E-08	2.449
INSIG2	ACTIVATED	8.24E-09	2.384
FGF19	ACTIVATED	1.18E-17	2.365
EPAS1	ACTIVATED	1.12E-08	2.349
LEP	ACTIVATED	9.29E-19	2.313
CYP3A	ACTIVATED	3.58E-07	2
HOXA10	ACTIVATED	1.60E-08	2

Gene	Pred. Activation	p-value	Z-Score
HNF1A	INHIBITED	1.16E-08	-2.098
NR1I3	INHIBITED	7.86E-14	-2.134
SIRT	INHIBITED	8.51E-07	-2.236
PXR	INHIBITED	5.34E-12	-2.301
ARNTL	INHIBITED	7.30E-07	-2.403
NR1H2	INHIBITED	5.63E-07	-2.591
MLXIPL	INHIBITED	3.58E-17	-2.811
ZBTB20	INHIBITED	1.38E-18	-3
SREBF2	INHIBITED	2.02E-25	-3.391
SCAP	INHIBITED	4.19E-24	-3.432
SREBF1	INHIBITED	4.35E-26	-3.509
ATP7B	INHIBITED	8.20E-17	-3.742
ACOX1	INHIBITED	4.14E-28	-4.637

L

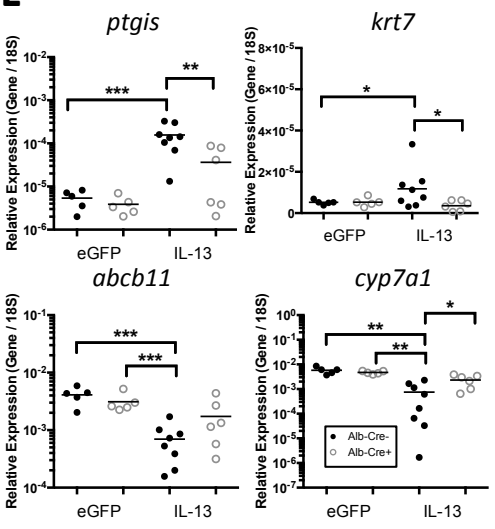

Figure 3

13-OP

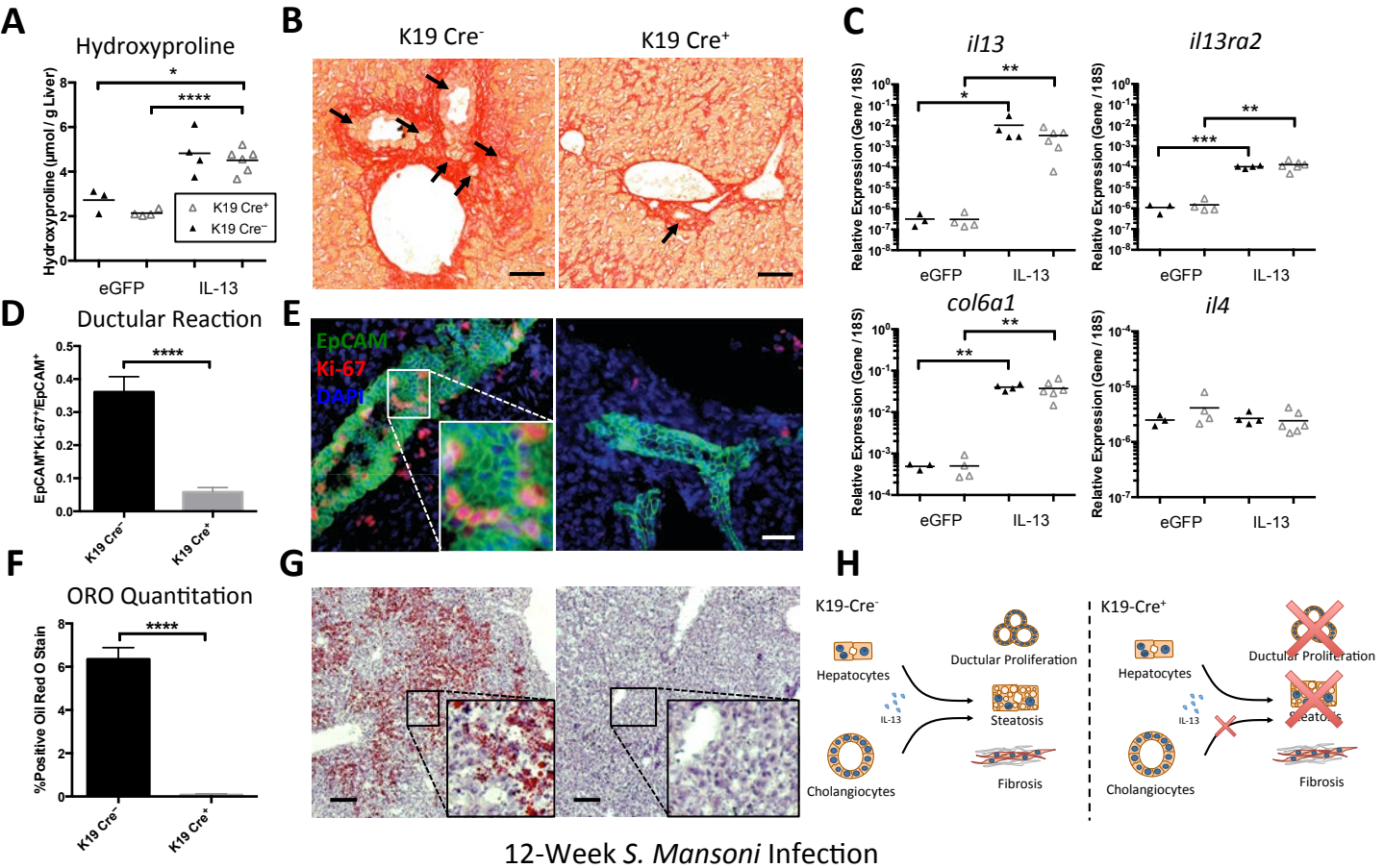

12-Week *S. Mansoni* Infection

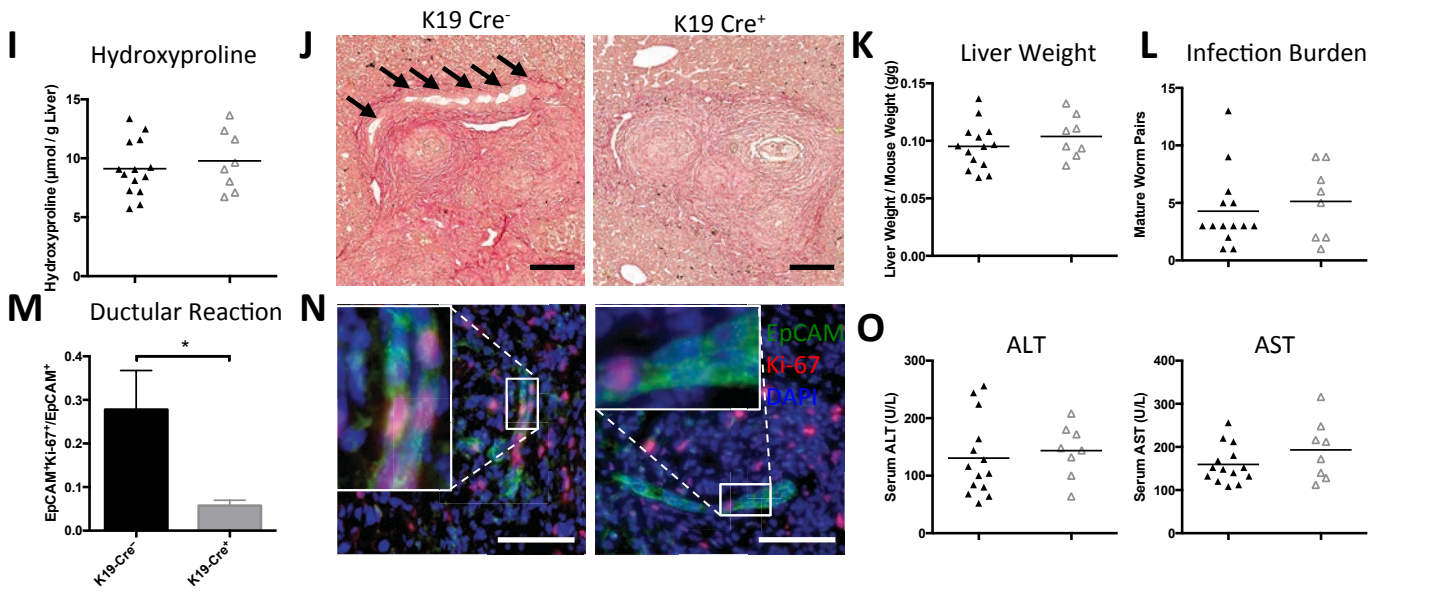

13-OP

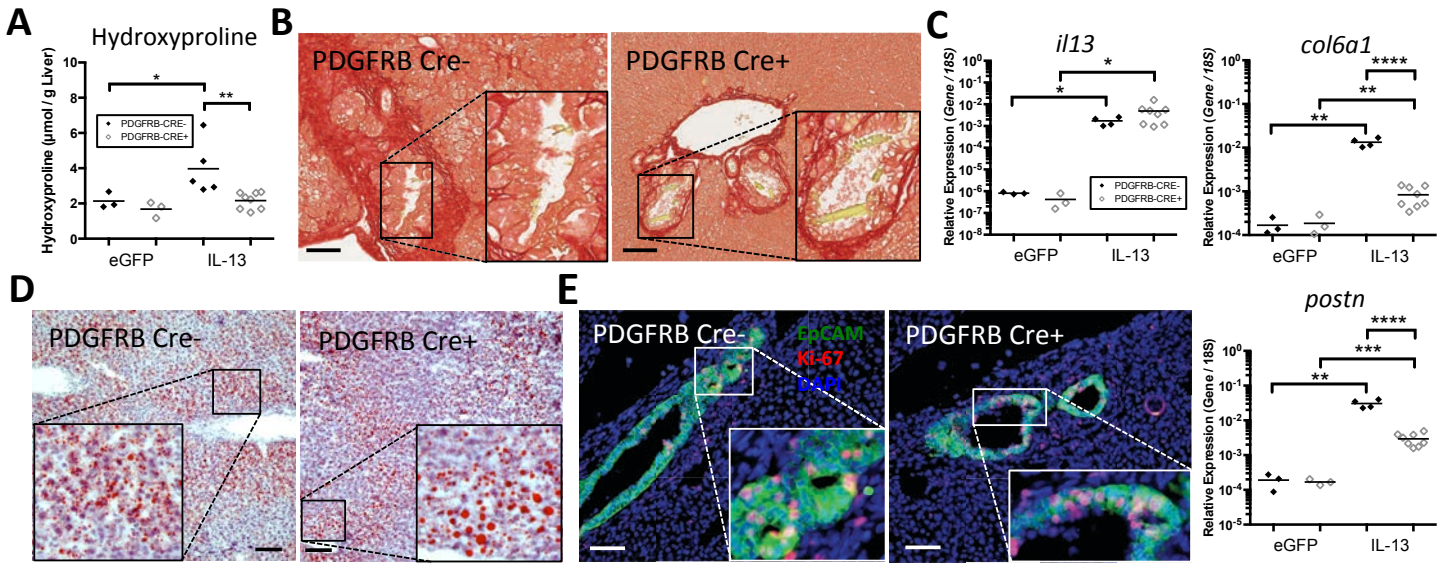

12-Week *S. Mansoni* Infection

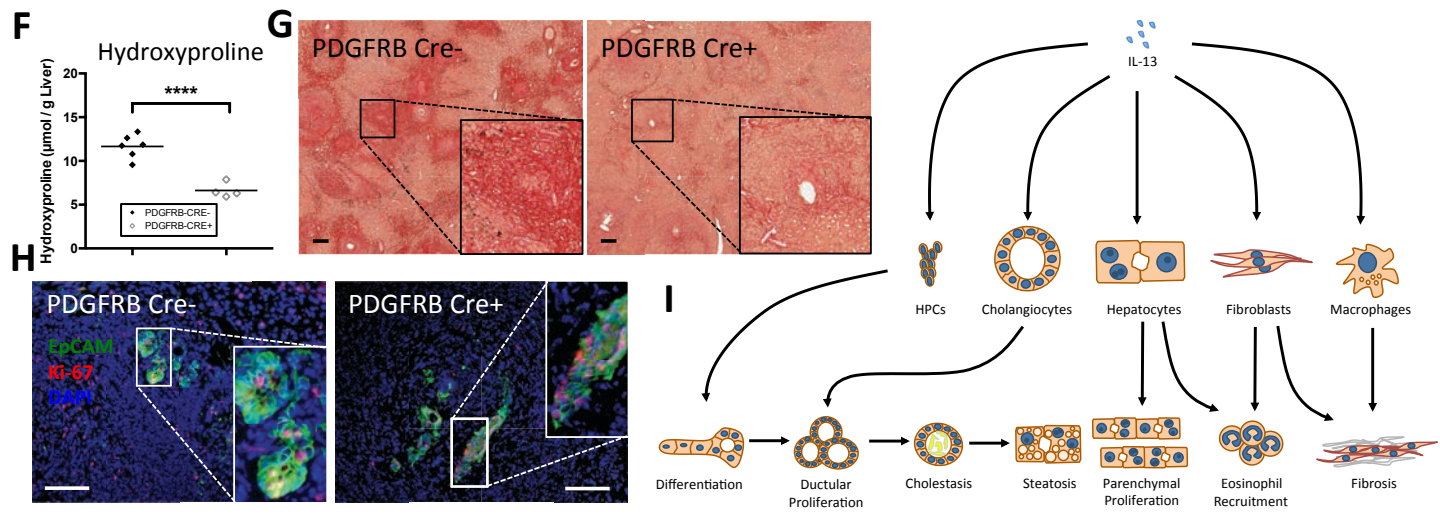

Figure 5

Revised Figure 6

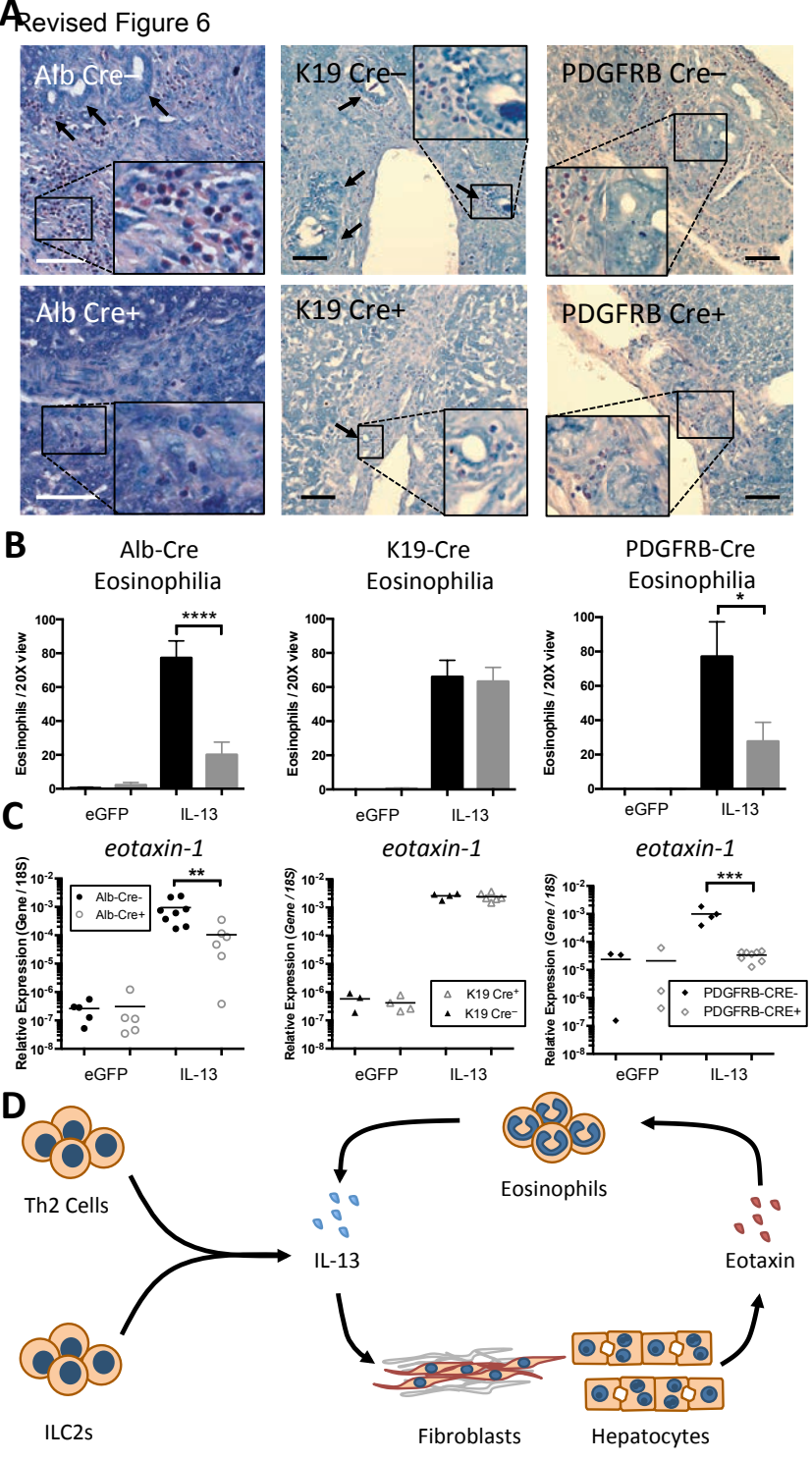

Figure 6

Revised Figure 7

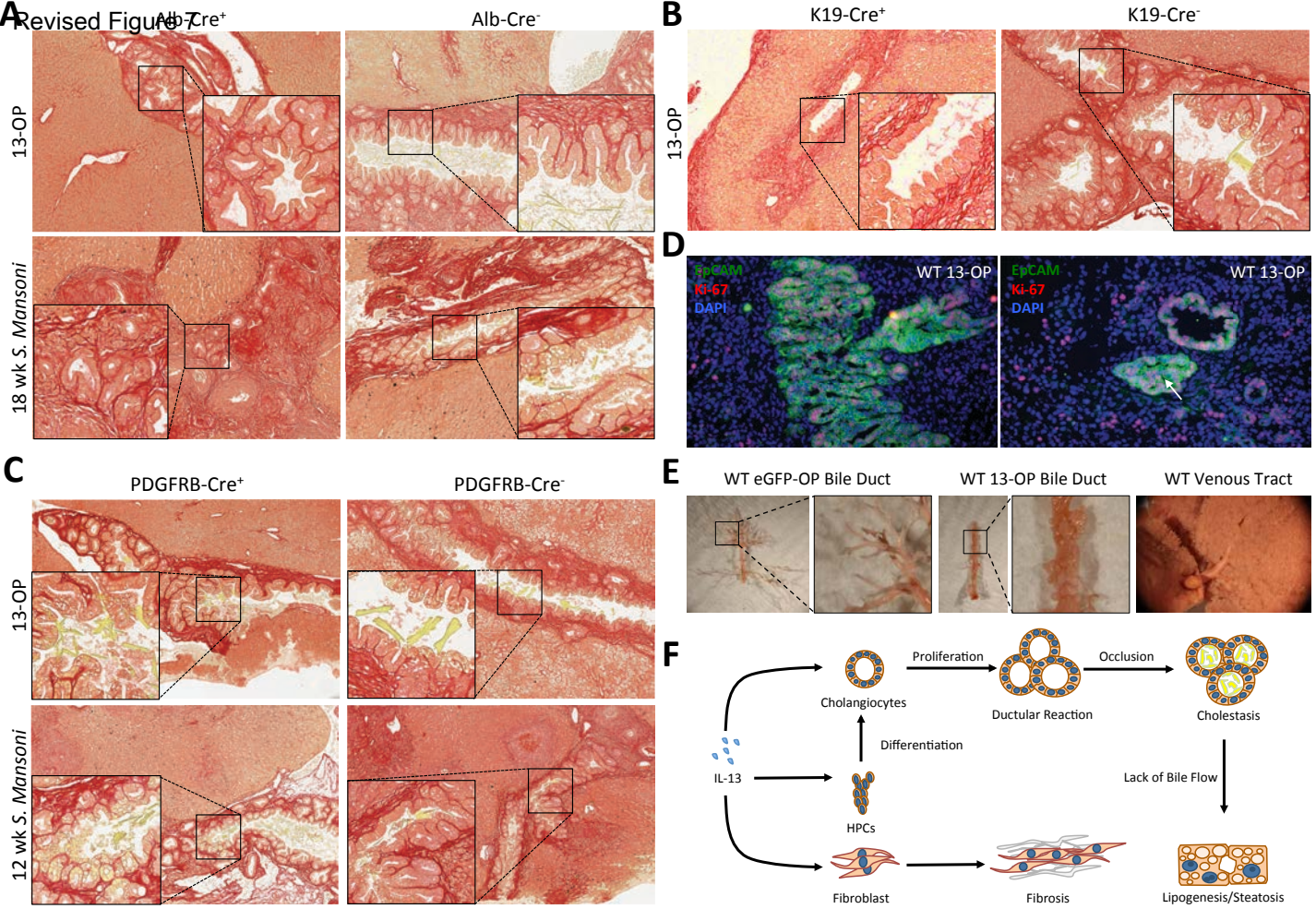

Figure 7

Supplementary Figure 1. Mortality and Infection Burden in Alb-Cre Mice During *S. mansoni* Infection.

(**A**) Survival of Alb-Cre mice during chronic *S. mansoni* infection. N-values Alb-Cre$^-$: n = 32; Alb-Cre$^+$ n = 30.

(**B**) Quantitation of infection burden by mature worm pair count from perfusate and egg count from KOH digested tissue. N-values Alb-Cre$^-$: n = 12; Alb-Cre$^+$ n = 11.

(Note) Results representative of three replicate experiments; p*<0.05, p**<0.01, p***<0.001, p****<0.0001.

Supplementary Figure 2. Mortality and Liver Damage in Alb-Cre Mice During 13-OP.

(**A**) Survival of Alb-Cre mice after 13-OP. N-values Alb-Cre$^-$: n = 10; Alb-Cre$^+$ n = 9. (Excluding mice deemed not over-expressing)

(**B**) Quantitation of serum ALT and AST levels after 13-OP. N-values Alb-Cre$^-$: n = 8; Alb-Cre$^+$ n = 6.

(Note) Results representative of two replicate experiments; p*<0.05, p**<0.01, p***<0.001, p****<0.0001.

Supplementary Figure 3. Efficiency of K19-CreERT Recombination

(**A**) Quantitation of percentage of EpCAM$^+$ cells expressing tdTomato R26R stop-floxed reporter. N-values left to right: n = 11, 11.

(**B**) Representative micrograph showing co-localization of EpCAM with tdTomato R26R stop-floxed reporter.

(Note) Data reported as mean ± S.E.M; p*<0.05, p**<0.01, p***<0.001, p****<0.0001.

Supplementary Figure 4. Mortality and Liver Damage in K19-Cre Mice During 13-OP.

(**A**) Survival of K19-Cre mice after 13-OP. N-values K19-Cre$^-$: n = 6; K19-Cre$^+$ n = 8.

(**B**) Quantitation of serum ALT and AST levels after 13-OP. N-values K19-Cre$^-$: n =4; K19-Cre$^+$ n = 5.

(Note) Results representative of two replicate experiments; p*<0.05, p**<0.01, p***<0.001, p****<0.0001.

Supplementary Figure 5. IL-13 Stimulation of Isolated HPCs.

(**A**) Murine HPCs isolated by $EpCAM^{+}Prom1^{+}CD24^{+}$ $TER119^{-}CD31^{-}CD45^{-}$ sorting develop noticeable morphological changes after IL-13 treatment.

(**B**) Assessment of cellular proliferation by Alamar Blue Reduction. (Data presented as mean ± SEM from 6 independent experiments.)

(**C**) Subset of Illumina Beadchip microarray analysis showing genes selected using the following criteria: $p < 0.05$ (Welch's t-test, Control v. IL-13), |Fold Difference| > 1.5 (Control v. IL-13).

(**D**) Select cholangiocyte differentiation and immune regulation markers significantly perturbed by IL-13 signaling on HPCs ($p < 0.05$).

Supplementary Figure 6. Mortality in PDGFRB-Cre Mice.

(**A**) Survival of PDGFRB-Cre mice after 13-OP. N-values $PDGFRB\text{-}Cre^{-}$: n = 8; PDGFRB $-Cre^{+}$ n = 10.

(**B**) Survival of PDGFRB-Cre mice during chronic *S. mansoni* infection. N-values $PDGFRB\text{-}Cre^{-}$: n = 11; $PDGFRB\text{-}Cre^{+}$ n = 7.

(Note) p*<0.05, p**<0.01, p***<0.001, p****<0.0001.

Supplementary Figure 7. Ki-67 Quantitation in PDGFRB-Cre Mice.

(**A**) Quantitation of percentage of $EpCAM^{+}$ cells per randomly chosen 20X microscopic field view expressing Ki-67 after 13-OP. N-values left to right: n = 8, 9.

(**B**) Quantitation of percentage of $EpCAM^{+}$ cells per randomly chosen 20X microscopic field view expressing Ki-67 after 12 week *S. mansoni* infection. N-values left to right: n = 8, 9.

(Note) Data reported as mean ± S.E.M. Results representative of two replicate experiments; p*<0.05, p**<0.01, p***<0.001, p****<0.0001.

Supplementary Figure 8. Type-2 Response in PDGFRB-Cre Mice During *S. mansoni* Infection. Quantitation of mRNA expression by qPCR of type-2 response genes relative to *18S* of PDGFRB-Cre mice after 12 week infection with *S. mansoni*.

(Note) p*<0.05, p**<0.01, p***<0.001, p****<0.0001.

Supplementary Figure 9. Assessment of Intrahepatic Steatosis.

Hall's bilirubin staining demonstrating lack of intrahepatic cholestasis in mice treated with 13-OP. (Green – bilirubin, yellow – counterstain, red – collagen)

Supplementary Figure 10. IL-33 is Not Required for DR during *S. mansoni* Infection.

(**A**) Wright-Giemsa staining of 12-week infected C57BL/6 control mice and IL-33-/- mice highlighting bile ducts.

(**B**) Quantitation of number of bile ducts pixels per randomly chosen 20X microscopic field view. Data is presented as mean ± SEM of 5 fields per mouse from at 5 mice per group.

(**C**) IL-13 mRNA quantitation by qPCR from 12 week infected mice. N-values left to right: n =

(**D**) Flow Cytometry results illustrating percentage of IL-13^{+} $CD4^{+}$ T cells from 12 week infected mice. N-values left to right: n = 5, 7, 9.

(Note) p*<0.05, p**<0.01, p***<0.001, p****<0.0001.

Supplementary Figure 11. PDGFRB-Cre Recombines with High Efficiency.

(**1**) E-Gel Low Range Quantitative DNA Ladder (Invitrogen). Ladder consists of 100ng x 2000 bp, 40 ng x 800 bp, 20 ng x 400 bp, 10 ng x 200 bp, 5 ng x 100 bp.

(**2-5**) Genotyping for IL4R native allele (not recombined, top band)

(**2**) PDGFB-Cre- sorted HSCs.

(**3**) PDGFB-Cre+ sorted HSCs.

(**4**) PDGFB-Cre- pre-sort.

(**5**) PDGFB-Cre- pre-sort.

(**6**) Ladder (see 1).

(**7-10**) Genotyping for IL4R KO allele (after recombination)

(**7**) PDGFB-Cre- sorted HSCs.

(**8**) PDGFB-Cre+ sorted HSCs.

(**9**) PDGFB-Cre- pre-sort.

(**10**) PDGFB-Cre- pre-sort.

(**11)** Ladder (see 1).

Revised Figure S1

Click here to download Supplemental Text & Figures Figure S1 High Def.pdf

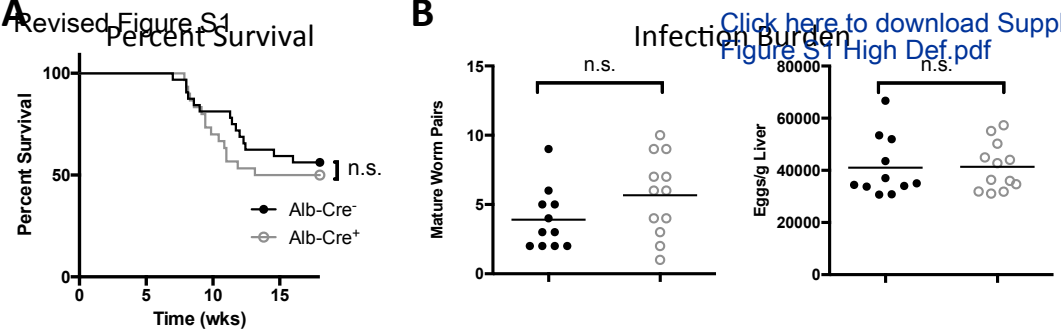

Figure S1

Revised Figure S2

Click here to download Supplemental Text & Figures Figure S2 High Def.pdf

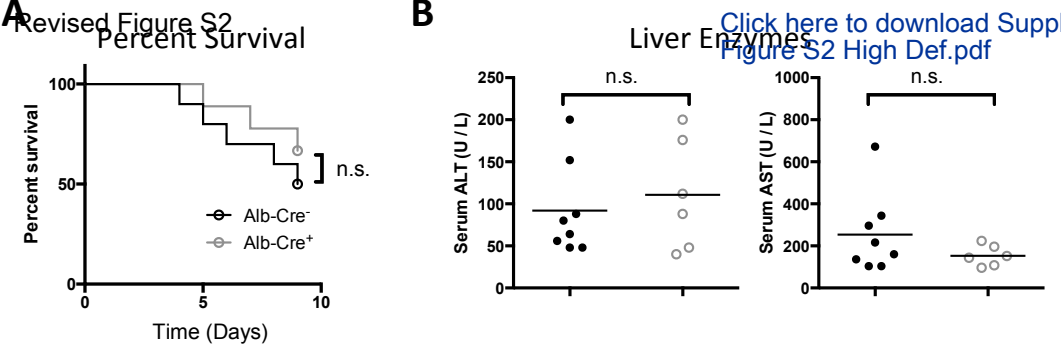

Figure S2

Revised Figure S3

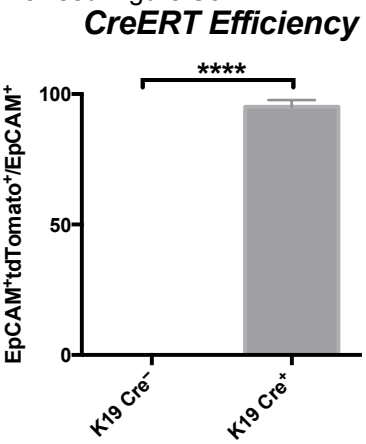

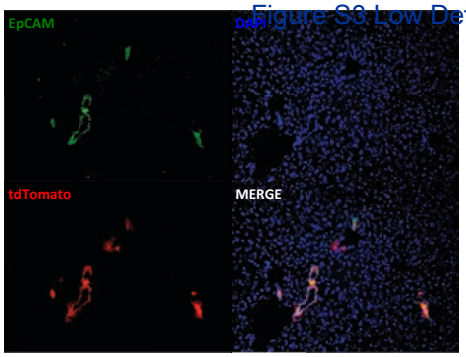

Click here to download Supplemental Text & Figures Figure S3 Low Def for Review.pdf

Figure S3

Revised Figure S4

Click here to download Supplemental Text & Figures Figure S4 High Def.pdf

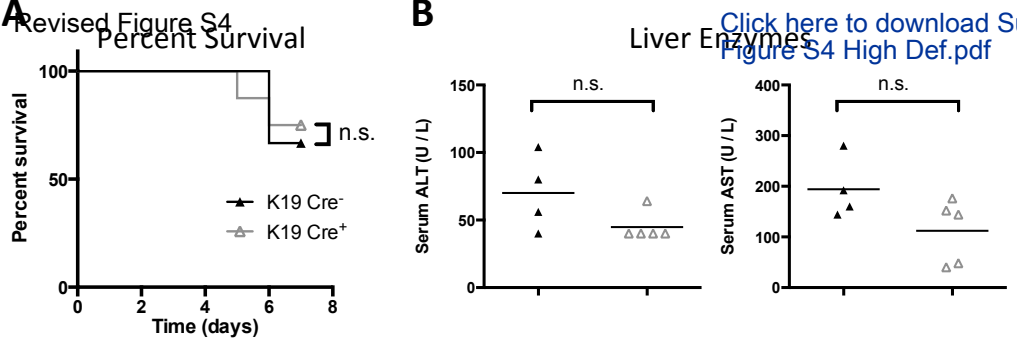

Figure S4

Revised Figure S5

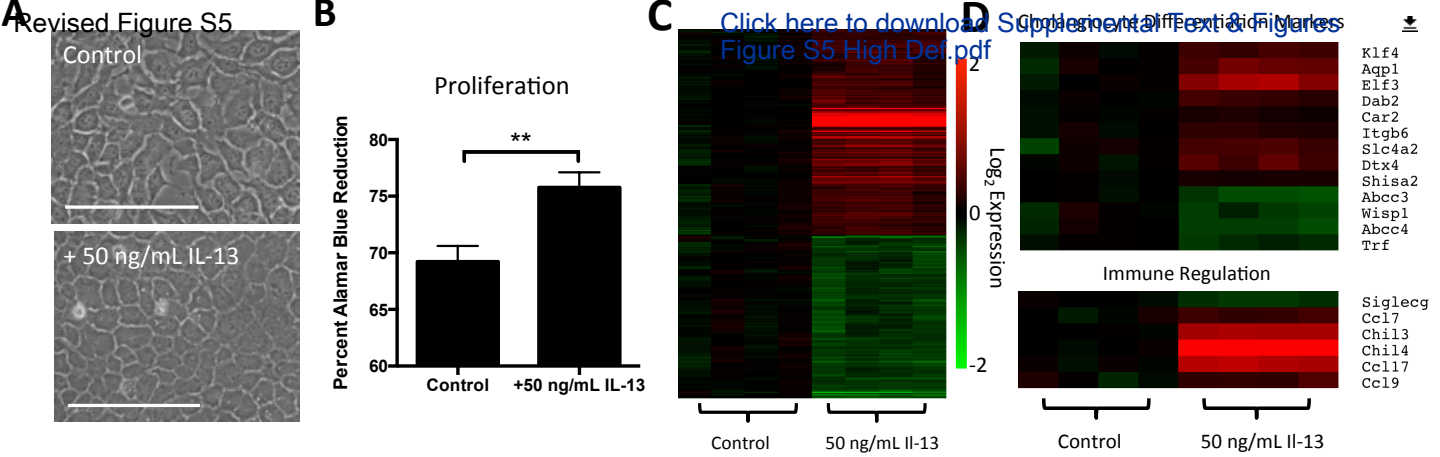

Figure S5

Revised Figure S6

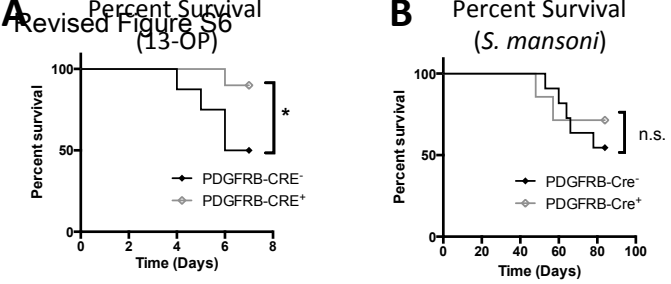

Click here to download Supplemental Text & Figures Figure S6 High Def.pdf

Figure S6

Revised Figure S7

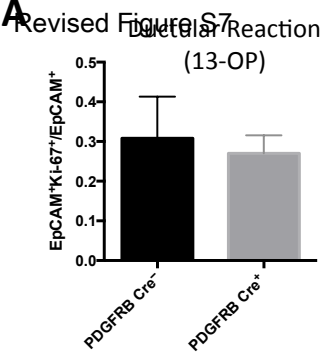

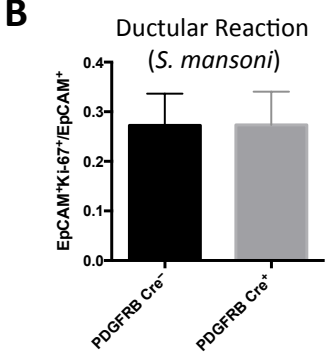

Click here to download Supplemental Text & Figures Figure S7 High Def.pdf

Figure S7

Revised Figure S8

Click here to download Supplemental Text & Figures Figure S8 High Def.pdf

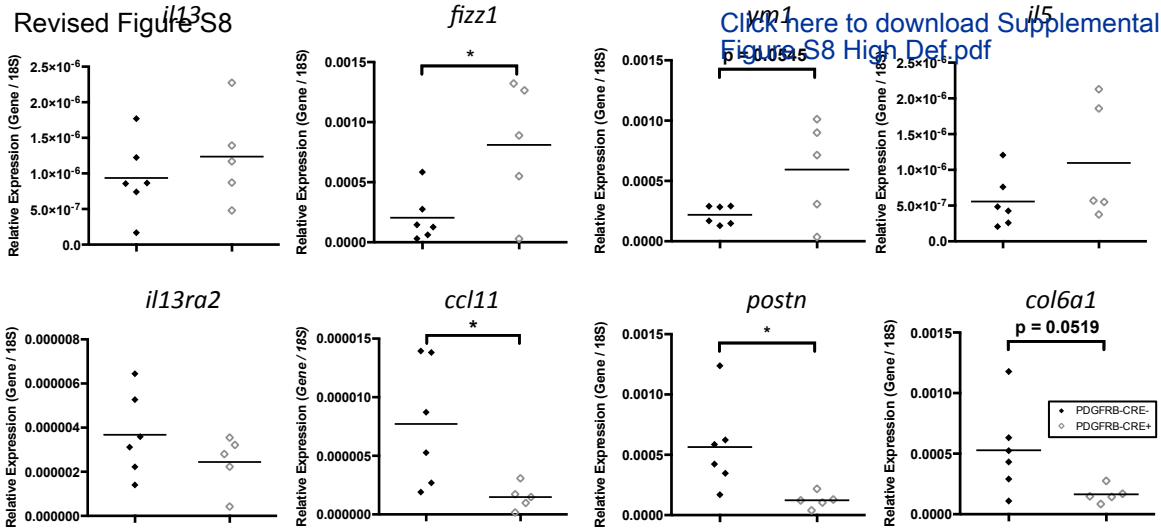

Figure S8

WT eGFT Of Hall's Bilirubin Stain

WT 15 Of Hall's Bilirubin Stain

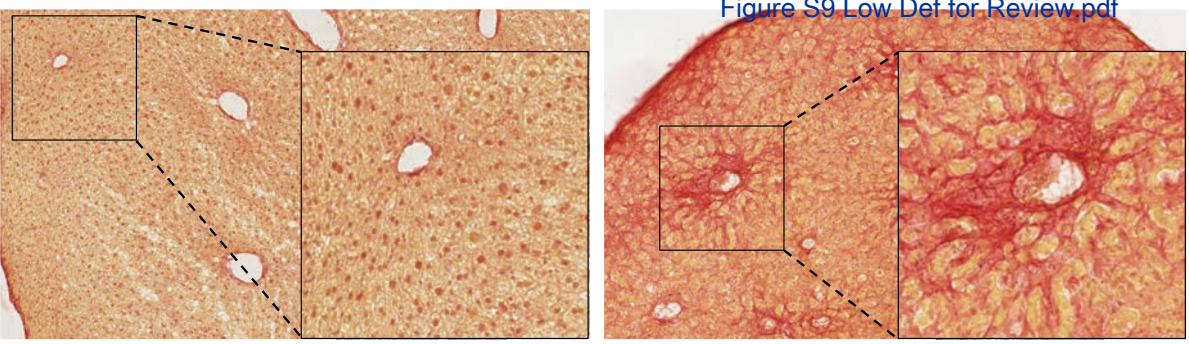

Figure S9

Revised Figure S10

Click here to download Supplemental Text & Figures
Figure S10 Low Def for Review.pdf

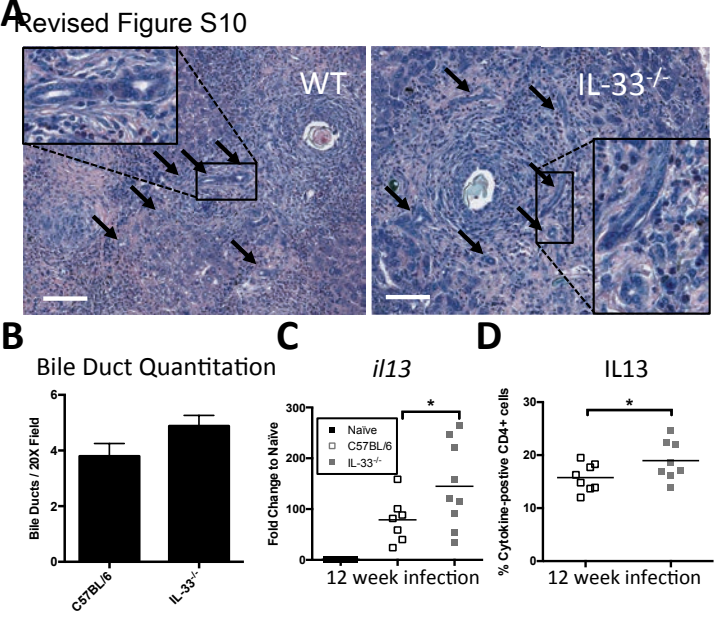

Figure S10

Figure S11

Supplementary Table 1. List of Primer Sequences for qPCR and PCR Genotyping

Gene	Forward Sequence 5'-3'	Reverse Sequence 5'-3'
ABCB11	ACATCTGTAGGGTTGTTGAGTG	CAAAGAAGCCAACTCGAGCG
CCL11	GAATCACCAACAACAGATGCAC	ATCCTGGACCCACTTCTTCTT
COL6A1	CGCCCTTCCCACTGACAA	GCGTTCCCTTTAAGACAGTTGAG
CYP7A1	TTCTGCGAAGGCATTTGGAC	TACATCCCTTCCGTGACCCA
FIZZ1	CCCTCCACTGTAACGAAGACTC	CACACCCAGTAGCAGTCATCC
IL13	CCTCTGACCCTTAAGGAGCTTAT	CGTTGCACAGGGGAGTCTT
IL13Ra2	CCTGGCATAGGTGTACTTCTTG	CCAAATAGGGAAATCTGCATCCA
IL4	ACGAGGTCACAGGAGAAGGGA	AGCCCTACAGACGAGCTCACTC
IL5	TGACAAGCAATGAGACGATGAGG	ACCCCCACGGACAGTTTGATTC
Periostin	CTGGTATCAAGGTGCTATCTGC	AATGCCCAGCGTGCCATAA
PTGIS	TGGGTTGAGAATCCTGCGG	CCACCAGCACAGTAAATATGTC
SPP1	CTGGCTGAATTCTGAGGGACT	TTCTGTGGCGCAAGGAGATT
YM1	CATGAGCAAGACTTGCGTGAC	GGTCCAAACTTCCATCCTCCA
Alb-Cre	GCGGTCTGGCAGTAAAAACTATC	GTCAAACAGCATTGCTGTCACTT
Alb-Cre Control	CTAGGCCACAGAATTGAAAGATCT	GTAGGTGGAAATTCTAGCATCATCC
IL4Ra-WT	GTACAGCGCACATTGTTTTT	CTCGGCGCACTGACCCATCT
IL4Ra-KO	GGCTGCCCTGGAATAACC	CCTTTGAGAACTGCGGGCT
K19-Cre	TTAATCCATATTGGCAGAACGAAAACG	CAGGCTAAGTGCCTTCTCTACA
tdTomato	AGATCCACCAGGCCCTGAA	GTCTTGAACTCCACCAGTAGTG